
Functional Cell Types in the Mouse Superior Colliculus

Ya-tang Li^{1,2,*}, Markus Meister^{1,3,*}

¹Division of Biology and Biological Engineering,

California Institute of Technology, Pasadena, CA 91125, USA

²Chinese Institute for Brain Research, Beijing 102206, China

³Tianqiao and Chrissy Chen Institute for Neuroscience,

California Institute of Technology, Pasadena, CA 91125, USA

*Correspondence: yatangli8@gmail.com, meister@caltech.edu

Abstract

The superior colliculus (SC) represents a major visual processing station in the mammalian brain that receives input from many types of retinal ganglion cells (RGCs). How many parallel channels exist in the SC, and what information does each encode? Here we recorded from mouse superficial SC neurons under a battery of visual stimuli including those used for classification of RGCs. An unsupervised clustering algorithm identified 24 functional types based on their visual responses. They fall into two groups: one that responds similarly to RGCs, and another with more diverse and specialized stimulus selectivity. The second group is dominant at greater depths, consistent with a vertical progression of signal processing in the SC. Cells of the same functional type tend to cluster near each other in anatomical space. Compared to the retina, the visual representation in the SC has lower dimensionality, consistent with a sifting process along the visual pathway.

1 Introduction

Parallel processing of information by the brain operates at three different levels: single neurons, cell types, and neural pathways. Processing of visual information at the cell-types level starts at the retina, where the signal is split into ~15 types of bipolar cells (Shekhar et al., 2016), ~63 types of amacrine cells (Yan et al., 2020), and ~40 types of retinal ganglion cells (RGCs) (Roska and Meister, 2014; Sanes and Masland, 2015; Baden et al., 2016). The RGCs send the processed information directly to the superior colliculus (SC), an evolutionarily conserved structure found in all vertebrates (Isa et al., 2021; Basso and May, 2017). The SC serves as an important visual center and also plays a vital role in coordinating animal behavior (Wheatcroft et al., 2022).

In the rodent, ~90% of RGCs project to the superficial layer of the SC (Ellis et al., 2016), and each SC neuron receives inputs from about six RGCs (Chandrasekaran et al., 2007). It remains unclear how the information is transformed at this stage and how many cell types exist in the SC. As in other brain areas, a solid classification of cell types in this circuit would support a systematic study of its function (Zeng and Sanes, 2017). By classic criteria of cell morphology and physiology, prior work has distinguished about five cell types in the retino-recipient superficial layer (Langer and Lund, 1974; May, 2006; Gale and Murphy, 2014; Wang et al., 2010; De Franceschi and Solomon, 2018). Differential expression of molecular markers has been used to describe about ten types in the superficial SC (Byun et al., 2016). By contrast, recent work on the primary visual cortex (V1) identified 46 types of neurons based on morphology and electrophysiology (Gouwens et al., 2019). Because the major inputs to the superficial SC are from the retina and V1, we hypothesize that the number of functionally distinct cell types in the SC has been underestimated.

34 The present work aims to identify functional cell types in the superior colliculus by virtue of their
35 responses to a large set of visual stimuli. These include a panel of stimuli that successfully separated
36 ~40 types of retinal ganglion cells, confirming many classes previously known from anatomical
37 and molecular criteria (Baden et al., 2016). By two-photon calcium imaging we recorded neuronal
38 responses from the posterior-medial SC of behaving mice while leaving the cortex intact. We classified
39 cell types based on their response to the high-dimensional visual stimulus using unsupervised learning
40 algorithms. We included several transgenic mouse strains that label subsets of SC neurons based
41 on gene expression patterns. The evidence points to ~ 24 functional types that come in two major
42 classes: one closely related to retinal responses, the other distinct. We report on the anatomical
43 organization of these functional types, their relation to molecular cell types, and their progression
44 throughout layers of the superficial SC. By comparing the space of visual features encoded in the
45 SC to that in the retina one finds that the superior colliculus already discards substantial information
46 from the retinal output.

47 2 Results

48 2.1 Single-cell imaging reveals diverse neuronal responses to a set of visual stimuli

49 To investigate the functional diversity of SC neurons, we imaged neuronal calcium responses to
50 a battery of visual stimuli using two-photon microscopy in head-fixed awake mice (Figure 1A).
51 To maintain the integrity of the overlying cortex, one is limited to the posterior-medial SC that
52 corresponds to the upper lateral visual field (Feinberg and Meister, 2015) (Figures 1B and 1C). We
53 recorded more than 5000 neurons from 41 image planes in 16 animals from different genetic lines,
54 including wild-type, Vglut2-Cre, Vgat-Cre, Tac1-Cre, Rorb-Cre, and Ntsr1-Cre mice. In the Cre
55 lines, the calcium indicator was restricted to the neurons expressing the respective transgene.

56 We presented a battery of visual stimuli (Figure 1D) chosen to probe spatio-temporal integration,
57 color-sensitivity, and movement processing (see Section 4.4 in Methods for detail). Included was a
58 "chirp" stimulus that modulates the intensity on the cell's receptive-field over both frequency and
59 amplitude; the full-screen "chirp" was previously employed in the classification of retinal ganglion
60 cells (Baden et al., 2016). Neurons in any given image plane showed robust and diverse responses
61 to these stimuli (Figures 1C-D). The animals were positioned on a circular treadmill but remained
62 stationary during most of the visual stimulation. Because locomotion barely modulates the visual
63 responses of SC neurons (Savier et al., 2019), we did not consider further the effects of movements.

64 2.2 Superficial superior colliculus comprises at least 24 functional cell types

65 To classify cell types based on their functional properties, we first performed a sparse principal
66 component analysis on the raw response traces (Figure 7A) (Mairal et al., 2009), which led to a
67 50-dimensional feature vector for each neuron. Then we added 4 designed features that describe
68 different aspects of the response: a habituation index (HI) computed from repeated stimuli, a direction
69 selectivity index (DSI), an orientation selectivity index (OSI), and a motion selectivity index (MSI,
70 see Methods). We focused on 3414 neurons that responded reliably to visual stimuli (signal-to-noise
71 ratio > 0.35, see definition in Methods Eqn 2), and searched for clusters in the 54-dimensional feature
72 space by fitting the data (3414 cells × 54 features) with a Gaussian mixture model, varying the
73 number of clusters in the mixture (Figure 2).

74 The quality of each clustering was assessed with the Bayesian information criterion (BIC), which
75 addresses concerns about overfitting by balancing the goodness of fit with generalizability. By this
76 measure the distribution of cells in feature space was best described with a Gaussian mixture of
77 24 components (Figure 2B), suggesting there are 24 functional types of neurons in the surveyed
78 population. Because the optimum in the BIC curve was rather broad (Figure 2B), and one could make
79 a case for both fewer or more clusters, we followed up by testing the stability of each cluster: We
80 fitted various sub-samples of the data set and assessed how well the resulting clusters correspond to
81 those in the full set, using a number of established statistics (see Methods and Figure 7). It emerged
82 that 3 of the 24 clusters are somewhat unstable (Figure 2D); they are marked as such in Figure 2A.
83 Overall the stability of the cluster definitions matched or exceeded those in related studies of neuronal
84 cell types (Gouwens et al., 2019; Baden et al., 2016). For the purpose of subsequent analysis we will
85 adopt this division into 24 types as suggested by the BIC.

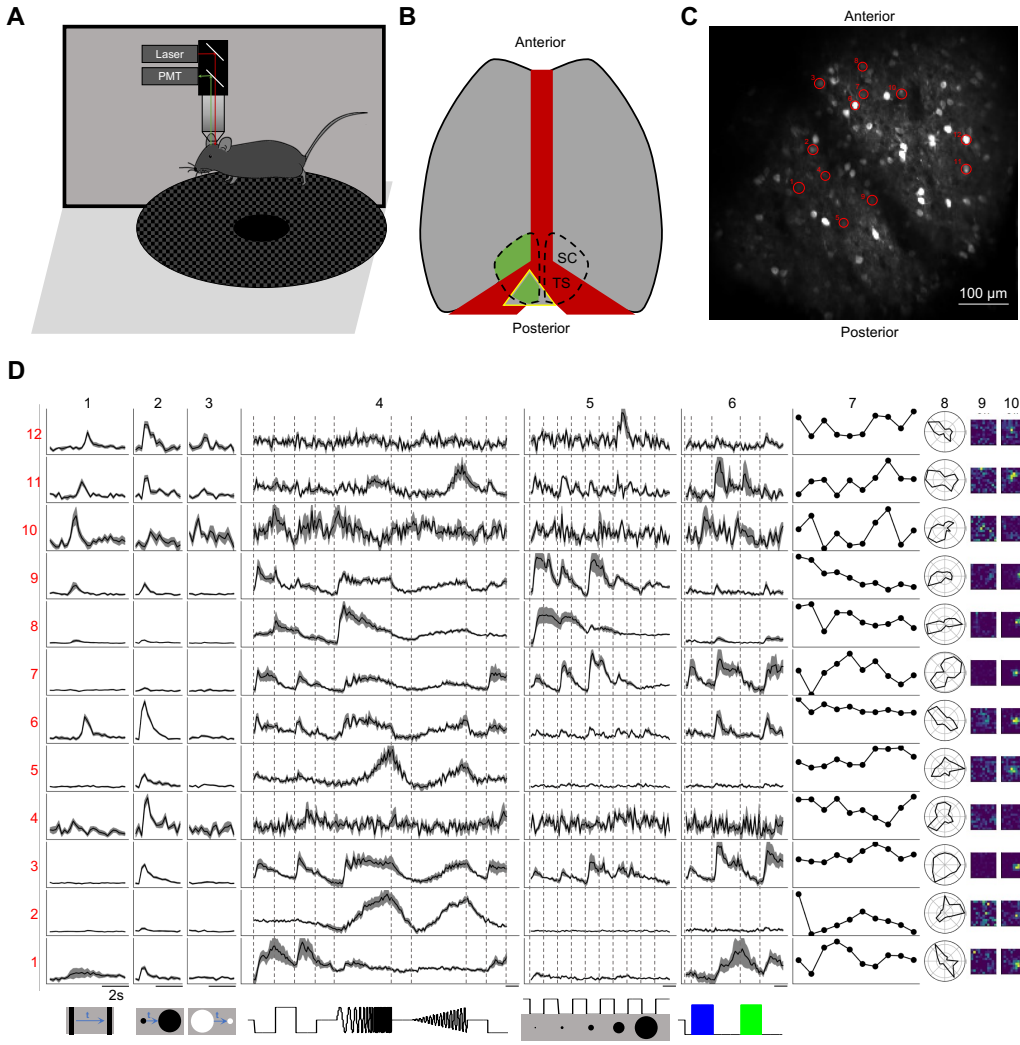


Figure 1: Two-photon imaging reveals diverse visual responses in awake mouse superior colliculus. **A.** Schematic of the experimental setup. Mice were head-fixed and free to run on a circular treadmill. Visual stimuli were presented on a screen. Neuronal calcium activity was imaged using two-photon microscopy. PMT, photomultiplier tube. **B.** Schematic of mouse brain anatomy after insertion of a triangular transparent plug to reveal the posterior-medial part of the superior colliculus underneath the transverse sinus. TS: transverse sinus. Yellow triangle indicates the plug. Green color indicates the expression of GCaMP6. **C.** A standard deviation projection of calcium responses to visual stimuli in one field of view. **D.** Response profiles of 12 neurons (rows) marked in C to visual stimuli in the bottom row. Columns 1-6 are time-varying calcium responses to a moving bar, expanding and contracting disks, a "chirp" stimulus with modulation of amplitude and frequency, spots of varying size, and blue and green flashes. Gray shading indicates the standard error across identical trials. Each row is scaled to the maximal response. Scale bars: 2 s. Subsequent columns show processed results: (7) response amplitude to an expanding black disc on 10 consecutive trials. (8) polar graph of response amplitude to moving bar in 12 directions. (9 and 10) Receptive field profiles mapped with small squares flashing On or Off.

86 The hierarchical relationship between these functional types is illustrated by the dendrogram in Figure
87 2A, which is based on the distances in feature space between cluster centers. The first branching of
88 the dendrogram splits the types into two groups (Figures 2A, 2C, 8 and 9), which we will call Group
89 1 (types 1-10) and Group 2 (types 11-24). Group 1 further splits into Group 1a (types 1-6) and 1b
90 (types 7-10).

91 Group 1 (types 1-10) is distinct from Group 2 (11-24) in that it responds more strongly to the chirp
92 stimuli (flashes and sinusoidal modulations in Figure 2A, 0.14 ± 0.05 vs. 0.04 ± 0.04 , $p < 0.001$,
93 two-sample t-test). All types in Group 1 prefer the expanding black disc over the receding white
94 disc. Almost all these types are excited by both On and Off stimuli in the chirp in the receptive field.
95 Also they prefer large spots to small spots, type 2 being a notable exception. Within Group 1, types
96 1-6 (Group 1a) are distinct from types 7-10 (Group 1b) in their response to sinusoid flicker: Group
97 1a prefers the low frequencies, whereas Group 1b responds over a wider range ($p=0.02$, Wilcoxon
98 rank-sum test). Type 7 in particular rejects the low flicker frequencies.

99 In Group 2, the response to chirp stimuli is generally weak compared to the moving stimuli. These
100 types respond well to small spots, unlike the Group 1 types. Other response properties in Group 2 are
101 more diverse, and some of these types have been noted previously. For example, Types 11 and 19
102 stand out in that moving stimuli suppress their activity (Ito et al., 2017). Several types (11, 15, 17)
103 are suppressed by the sinusoid flicker (Ito et al., 2017); 11 and 15 also show rebound after cessation
104 of that stimulus. Type 14 responds strongly to moving stimuli but hardly at all to the entire chirp.
105 Type 18 is remarkably insensitive to any moving stimulus.

106 What are the distinguishing features in their visual responses? Figure 3B distills the responses to
107 the stimulus palette into 15 indices (see Methods) that help to characterize each type (only values
108 significantly different from zero are shown, see Figure 10A for all values). For some indices, Figure
109 3A shows violin or bar plots for each type. As a rule, almost all the types are sensitive to moving
110 stimuli, like the traveling dark bar and the expanding black disc (RtM in Figure 3B). For many types,
111 these were the stimuli that elicited the strongest response.

112 Some of these features of the visual response were highly correlated with each other ($p<0.05$), in that
113 they co-varied in the same or opposite directions across types (Figures 3C and 10B). For example,
114 direction selectivity (DSI) and orientation selectivity (OSI) tend to be strong in the same cell type
115 (types 9, 14, 20, 24). Another strong correlation exists between the preferred stimulus size (BSS) and
116 the response during recovery from the frequency and amplitude chirps (RaFM and RaAM).

117 2.3 Neurons of the same type cluster in anatomical space

118 In the retina, ganglion cells come in ~40 different types (Sanes and Masland, 2015), and they tile the
119 surface in a so-called mosaic arrangement. Neurons of the same type are spaced at regular distances
120 from each other. Neurons of different types are distributed more or less independently (Roy et al.,
121 2021); therefore a ganglion cell's nearest neighbor is almost always of a different type. The presumed
122 purpose of this arrangement is to ensure uniform coverage such that every location in the visual field
123 has access to each of the types of retinal ganglion cell. Because the retina projects directly to the SC,
124 we investigated whether neurons there are also organized for uniform coverage.

125 Figure 4A illustrates SC neurons in a single image plane, labeled according to functional type (for
126 more examples see also Figure 11A). Several features are immediately apparent. First, cells of a
127 given type do not repel each other; in fact, the nearest neighbor is often a neuron of the same type.
128 Second, the types don't cover space uniformly. Some types are segregated from each other (e.g., 7
129 and 21) whereas others overlap in space (e.g. 14 and 24).

130 To pursue these spatial arrangements in greater detail, we computed for each functional type the
131 spatial autocorrelation function (also called "density recovery profile"): This is the average density of
132 neurons plotted as a function of distance from another neuron of the same type (Zhang et al., 2012;
133 Rodieck, 1991). When applied to retinal ganglion cells, this function shows a pronounced hole of
134 zero density at short distances. Here, instead, the density remains high down to a distance of 10 μm ,
135 which is the typical diameter of a soma (Figure 4B). In fact for several of these SC types the density
136 is highest just 1-2 cell diameters away.

137 Over larger distances, the autocorrelation function decays gradually (Figure 4C), whereas one would
138 expect a flat curve if the cells appeared at uniform density. The density drops to half the peak value

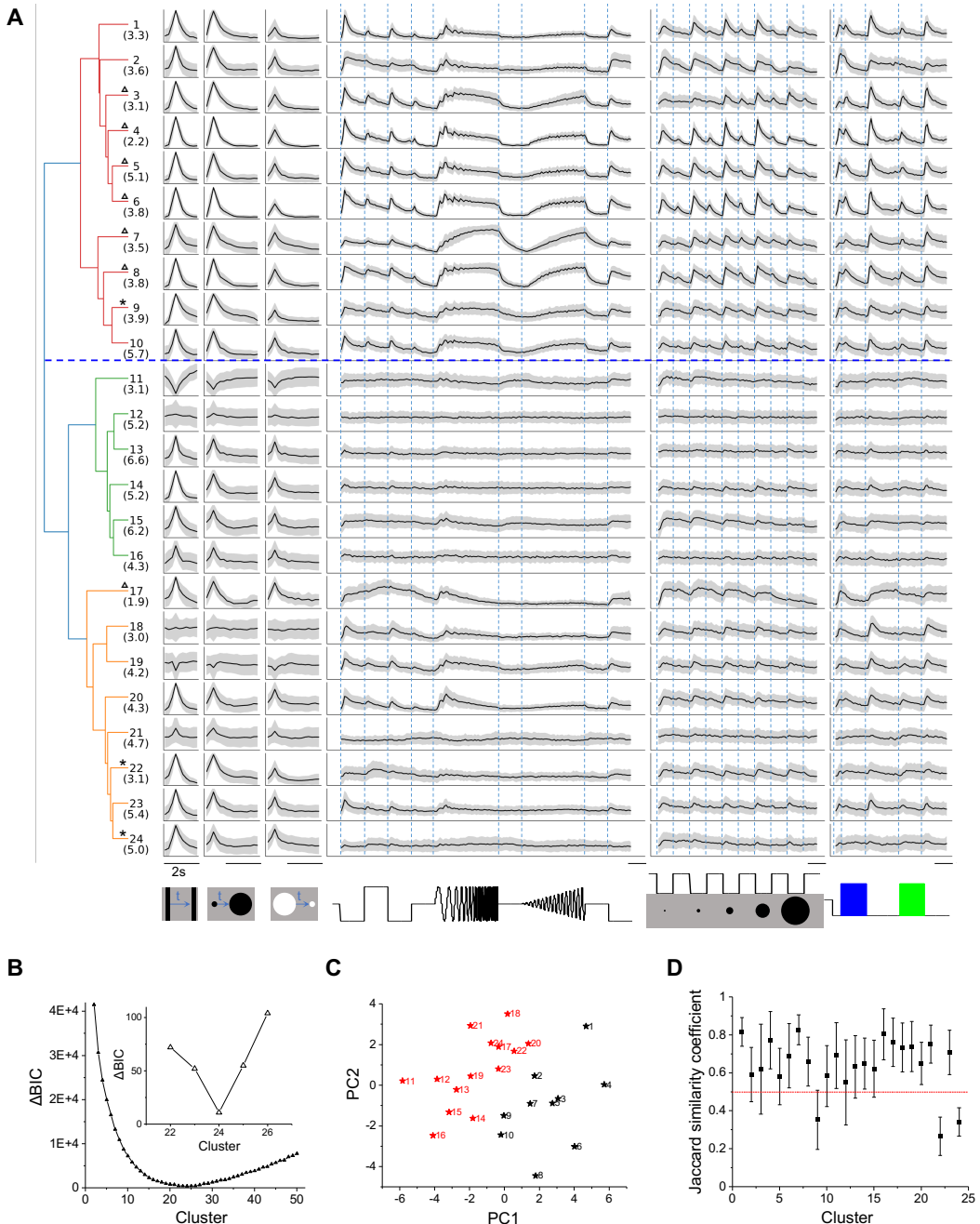


Figure 2: Twenty-four functional cell types in the mouse SC. **A.** Dendrogram of 24 clusters based on their distance in feature space. For each type this shows the average time course of the neural response to the stimulus panel. Grey: standard deviation. The vertical scale is identical for all types and stimulus conditions. Blue dashed line separates groups 1 and 2. Numbers in parentheses indicate percentage of each type in the dataset. Stars mark the unstable clusters with $JSC < 0.5$ (see panel D). Triangles mark the clusters where more than half neurons are contributed by one mouse. Scale bars: 2 s. **B.** Relative Bayesian information criterion (ΔBIC) for Gaussian mixture models with different numbers of clusters. **C.** The center of each cluster in the first two principal axes of feature space. Black and red colors label Groups 1 and 2 respectively. **D.** Jaccard similarity coefficient (JSC) between the full dataset and subsets (Mean \pm SD).

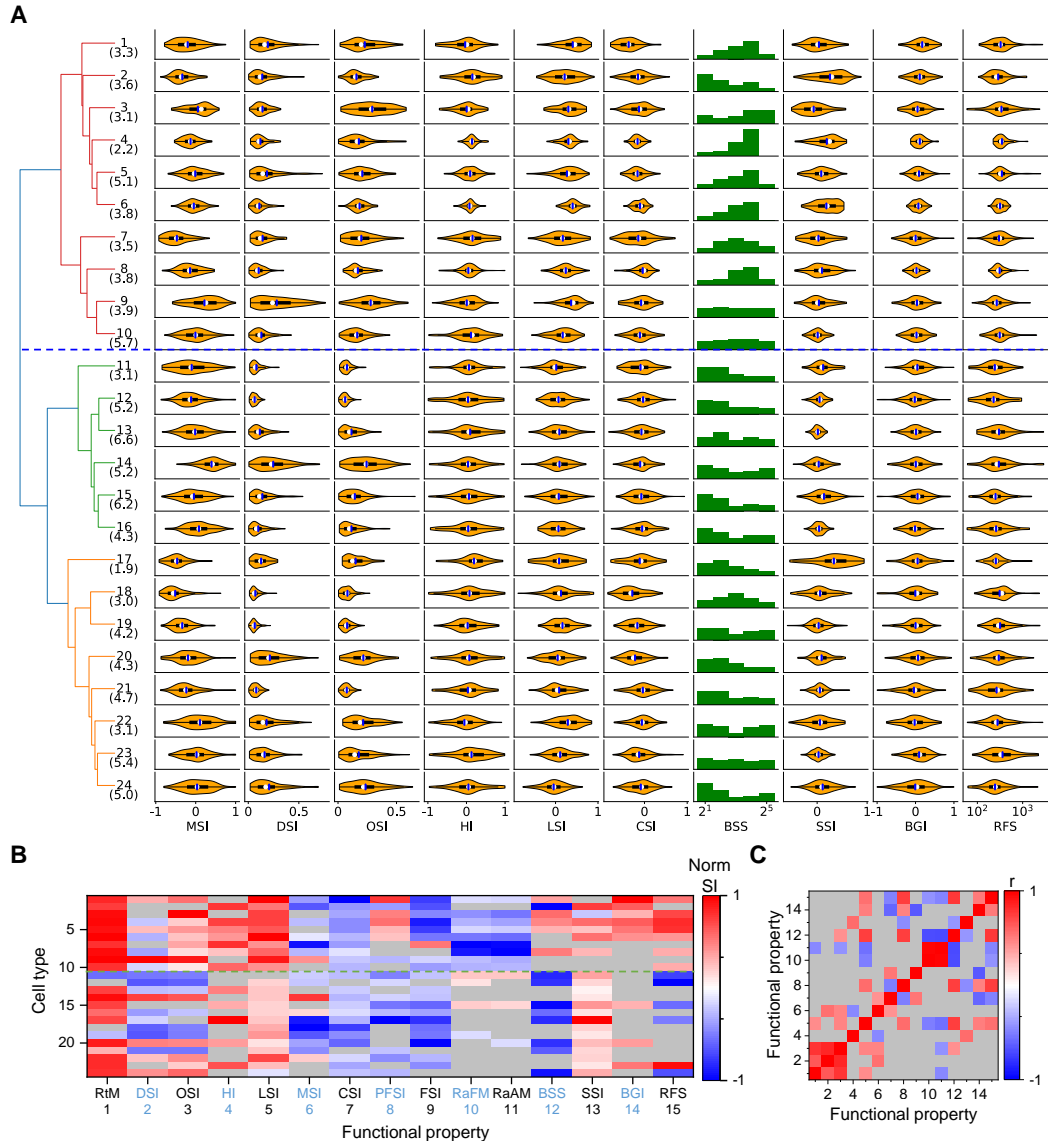


Figure 3: Functional diversity among different types. **A.** Violin plots or histograms of various response indices: motion selectivity index (MSI), direction selectivity index (DSI), orientation selectivity index (OSI), habituation index (HI), looming selectivity index (LSI), contrast selectivity index (CSI), best stimulus size (BSS), surround suppression index (SSI), blue green index (BGI), and receptive field size (RFS). Blue dashed line separates Group 1 and Group 2. **B.** Normalized selectivity index (SI, normalized for each column) of functional properties represented by different cell types (See Methods). RtM: response to motion; PFSI: peak-final selectivity index; FSI: frequency selectivity index; RaFM: response after frequency modulation; RaAM: response after amplitude modulation. Grey: values that are not significantly different from 0 ($p \geq 0.05$, one-sample t-test). Green dashed line separates Group 1 and Group 2. **C.** Pearson's correlation coefficients of the representation between pairs of functional properties. Grey: non-significant correlations ($p \geq 0.05$).

139 at a radius of 150-250 μm . This suggests that neurons of a given type form patches of 300-500 μm
140 diameter. Note this accords with a similar patchy organization found previously for certain functional
141 parameters, like the preferred orientation (Feinberg and Meister, 2015) or preferred direction of
142 motion (de Malmazet et al., 2018; Li et al., 2020).

143 We considered a potential source of error that could give the mistaken appearance of a patchy
144 organization: A functional type might fortuitously be limited to just one recording session, owing to
145 some peculiarity of that animal subject, and so would appear only in the visual field covered during
146 that session. This is not the case: Figure 12 shows that recordings from different mice confirm the
147 same functional type. Furthermore, a single recording session reveals separate patches of different
148 types (Figures 4A and 11A).

149 An important scale by which to judge this spatial organization is the size of the receptive field (RF).
150 In the retina, the mosaic arrangement spaces the ganglion cells about one RF diameter apart, so that
151 the RFs of neurons from the same type have little overlap. In the SC that is clearly not the case.
152 From the autocorrelation functions (Figure 4B) we compared the average density of cells within 0.5
153 RF diameters to the density at 0.5-1.0 RF diameters. In the SC, that ratio is greater than 1 for all
154 functional types and often close to 2 (Figure 4D). By comparison, for the W3 type of retinal ganglion
155 cell (Zhang et al., 2012) that ratio is only 0.4.

156 In the retina, the arrangement of one functional type is almost entirely independent of the other
157 types (Wassle et al., 1981) (but see Roy et al., 2021). In the SC we found a strong anticorrelation:
158 Within 50 μm of a given cell, the cells of the same type occurred at greater-than-average density, but
159 cells of the other types at lower density (Figure 4E). One might say that each functional type tends to
160 displace the others. To illustrate this further, we calculated the normalized distance between all pairs
161 of cell types (Figure 4F). Twenty-one types show significant spatial separation from at least one other
162 cluster (Figures 11B, p<0.05, bootstrap analysis).

163 The functional properties of neurons also varied along the depth axis of the superior colliculus (Figure
164 4G). The individual response parameters changed in only subtle ways; for example one can find
165 more neurons with larger receptive fields at greater depth but on average deeper neurons preferred
166 smaller spot stimuli. However, at the level of identified types (which takes many response parameters
167 into account) the differences were more pronounced. In particular, neurons in the upper 100 μm
168 were composed primarily of types 1-10 (Group 1, 56%) while neurons deeper than 100 μm belonged
169 primarily to types 11-24 (Group 2, 68%, p<0.001, chi-square test, Figures 4H, 11C-D).

170 2.4 Genetically labeled populations comprise multiple functional types

171 Several experiments focused on superior colliculus neurons with specific molecular identity, taking
172 advantage of existing mouse Cre-lines (Figure 5). The Vgat-Cre and Vglut-Cre lines respectively
173 label GABAergic and glutamatergic neurons; Tac1-Cre labels populations of neurons stratified in
174 the superficial SC (Harris et al., 2014), Rorb-Cre labels both excitatory and inhibitory neurons in the
175 superficial sublayer (Byun et al., 2016; Gale and Murphy, 2018); finally Ntsr1-Cre labels a subtype
176 of excitatory neurons that have a wide-field morphology at deeper locations (Gale and Murphy, 2014,
177 2016, 2018).

178 Some systematic differences between these genetically labeled populations are apparent already
179 from the chirp responses (Figure 5A). For example, excitatory and inhibitory neurons differ at the
180 population level: Vglut+ neurons prefer flashed over moving stimuli and spots of small size, whereas
181 Vgat+ neurons respond equally to flashed and moving stimuli and prefer large-size spots (Figure
182 5B). Tac1+ neurons have the highest direction selectivity and small receptive fields, whereas Ntsr1+
183 neurons show strong orientation selectivity. We refrain from analyzing the fine-grained distribution
184 of the 24 functional types in each genetic population, because the experiments did not cover every
185 combination of genetic label and depth and visual field location, leading to possible confounds.

186 Prior reports on the Ntsr1+ neurons suggest that they are of the distinctive wide-field anatomical
187 type, with a broad dendritic fan (Major et al., 2000), and that they have the largest receptive fields in
188 the superficial SC (Gale and Murphy, 2014). In fact, we did find very large receptive fields among
189 Ntsr1+ neurons, but surprisingly also many small ones (Figure 5C). Notably another recent study
190 also reported a large variation of receptive field sizes in this line (Hoy et al., 2019). Perhaps some of
191 the Ntsr1+ neurons have the wide-field morphology but are dominated by just one or a few dendritic
192 inputs.

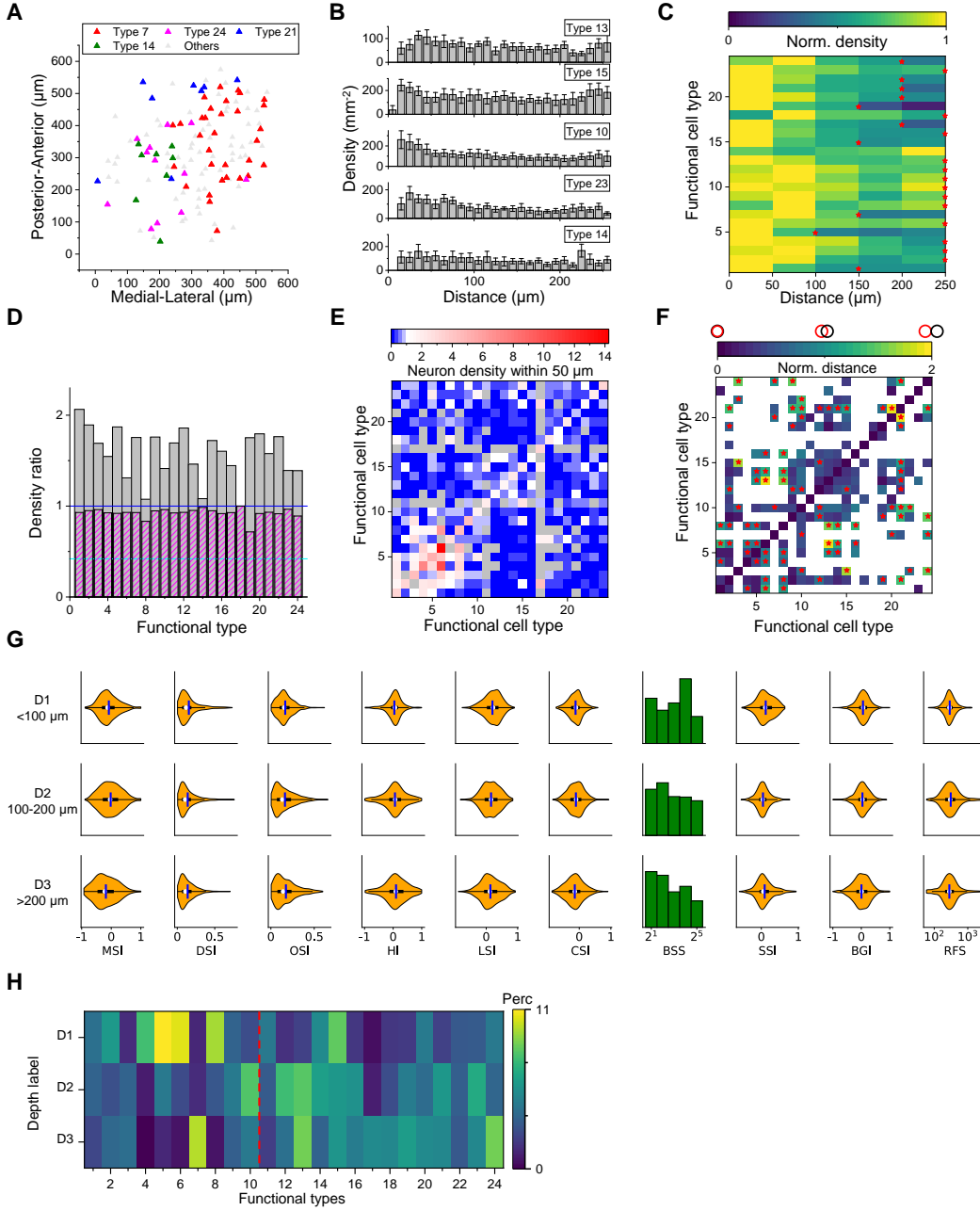


Figure 4: Spatial organization of functional cell types. **A.** Anatomical locations of four types of neurons from one sample recording. **B.** Averaged density recovery profile (DRP) of five example types for all imaging planes. Error bars denote SEM. **C.** Density of neurons of a given functional type at various distances from a neuron of the same type. Red stars mark the smallest radius within which the neuron density is larger than half of the peak density. **D.** Decay of the DRP for each functional type. Gray bars: the ratio between the density at a distance of 0-0.5 RF diameters and the density at 0.5-1 RF diameters. Magenta bars: Same but for cells from all the other types. Cyan line: The value for W3 retinal ganglion cells (Zhang et al., 2012). **E.** Density of neurons from different functional types (columns) within $50 \mu\text{m}$ of a given neuron whose type is indicated by the row. Note the largest density is for cells of the same type except types 8, 11 and 16. Grey: insufficient data to estimate density. **F.** Normalized anatomical distance between neurons in any two functional types. Red stars indicate significant separation ($p < 0.05$, bootstrap analysis). White: insufficient data. **G.** Functional properties of neurons in three ranges of depth. Display as in Figure 3A. **H.** The percentage of functional types in each depth range. Red dashed line separates Group 1 and Group 2.

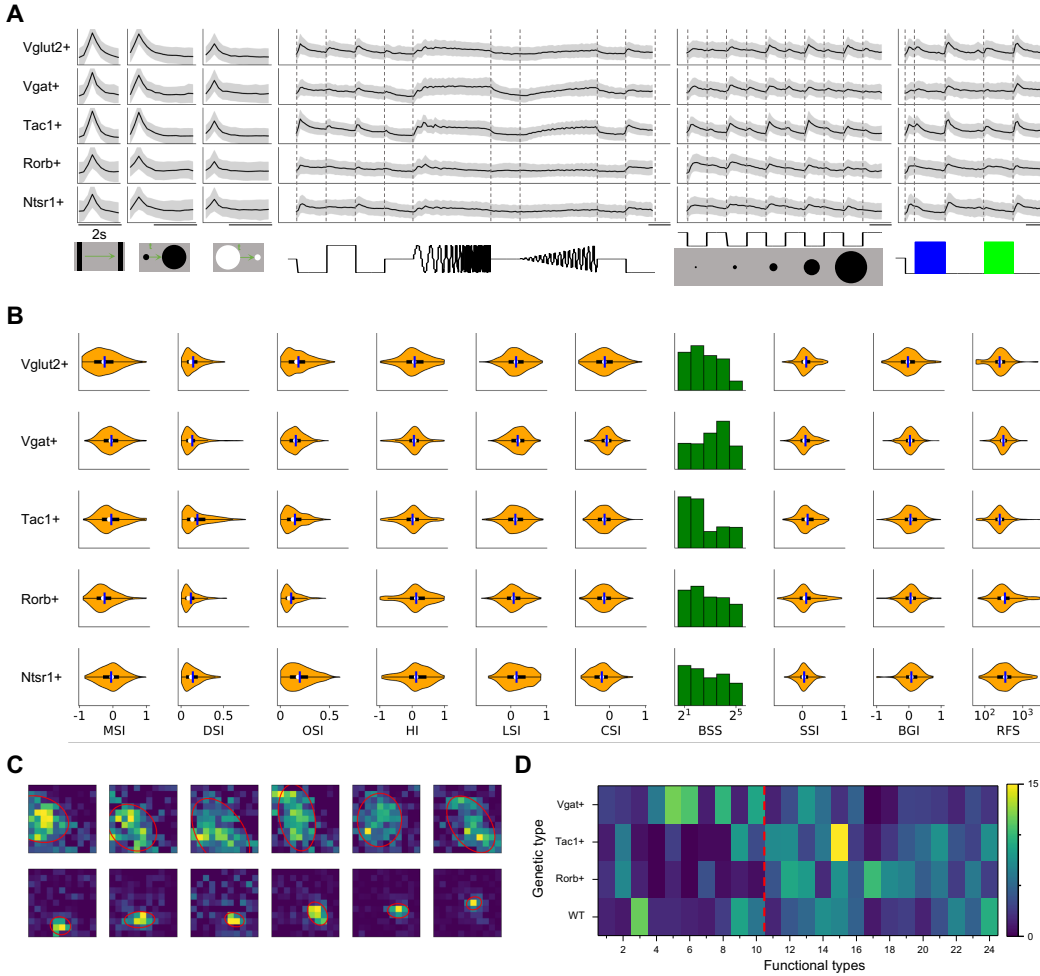


Figure 5: Functional properties in genetically labeled populations. **A.** Average response to the chirp stimulus of five genetically labelled cell types. Display as in Figure 2A. **B.** Functional properties of the genetically labelled types. Display as in Figure 3A. **C.** Example receptive fields of Ntsr1+ neurons mapped with squares flashing Off and fitted with an ellipse. **D.** The percentage of functional types in mice with different genetic backgrounds. Red dashed line separates Group 1 and Group 2.

193 At the level of functional classification, two features stand out (Figure 5D): First the inhibitory
 194 neurons are more represented by types in Group 1 (types 1-10, 58%). Second the Rorb+ and Tac1+
 195 neurons comprise mostly the functional types of Group 2 (types 11-24, 77% and 82% respectively).
 196 Recall that these types respond poorly to the simple chirp stimulus but strongly to moving and
 197 expanding objects (Figure 2A). Beyond that, there is no one-to-one relationship between genetic
 198 labels and functional properties: Each of these genetic markers labels neurons with various functions,
 199 and vice versa.

200 2.5 Transformations from retina to superior colliculus

201 The superficial layers of the superior colliculus receive direct input from most types of retinal ganglion
 202 cells. How is visual information transformed as the superior colliculus processes these signals further?
 203 To address this directly, our experimental design included a precise copy of the stimuli used previously
 204 to classify and distinguish functional types of retinal ganglion cells (Baden et al., 2016). Here we
 205 compare the known retinal ganglion cell response types to those we identified in superior colliculus.
 206 As a first-order analysis, we fitted the chirp and color responses of each SC type with a linear
 207 combination of the responses of RGC types (Figures 6A, 13A-D) (Rosón et al., 2019). Under the null

208 hypothesis where each SC type is dominated by one RGC type, this should yield fit weights only
209 along the diagonal. Instead, the optimal fit mixes contributions from many RGC types. While these
210 coefficients cannot be interpreted as representing synaptic connectivity, they nonetheless indicate a
211 broad mixing of retinal inputs at the level of superior colliculus.

212 A number of interesting features emerge. First, some RGC types have universally excitatory (types 16
213 (ON DS trans.) and 23 (ON ‘mini’ alpha)) or universally inhibitory (types 7 (OFF sustained) and 18
214 (ON transient)) effects on almost all the SC responses. The inhibitory effects could be implemented
215 by recruiting local inhibitory neurons in SC. These RGC types represent a diversity of functional
216 properties. Second, 18 of 32 RGC types have significantly larger contribution to Group 1 (types
217 1-10) than Group 2 (11-24, $p < 0.05$, two-sample t-test). Recall that these groups represent the major
218 division in the dendrogram of SC types (Figure 2A).

219 Another substantial transformation from retina to colliculus occurs in the representation of orientation
220 and direction for moving stimuli. In the retina, different ganglion cell types are used to encode the
221 direction vs the orientation of bar stimuli (Figures 6B, 13E). By comparison, in the colliculus it
222 appears that the same cells are selective for orientation and for direction (Figures 6C, 13F-I). Similarly,
223 the retina contains many ganglion cell types with purely On-type or Off-type responses (Sanes and
224 Masland, 2015; Baden et al., 2016). By comparison, at the level of the colliculus those two pathways
225 are largely combined, and most functional types are of the On-Off type with a bias towards Off
226 responses (Figure 2A). These examples suggest a reduction in diversity during transformation from
227 retina to colliculus. To test this more globally, we subjected the entire set of chirp-color responses to
228 a principal component analysis, and compared the results from RGC types to those from SC types
229 (Figure 6D). In the superior colliculus, the variance in the visual responses can be explained by
230 fewer principal components than in the retina. This suggests a reduction in diversity from retina
231 to colliculus, as might be expected from selective visual filtering of features essential to guide the
232 animal’s behavior.

233 3 Discussion

234 Parallel pathways are central to the architecture of biological vision. The visual pathway forks already
235 at the photoreceptor synapse – into ON and OFF representations – and by the time the signal emerges
236 from the eye it has been split into about 40 channels. Each of these pathways is carried by a type
237 of retinal ganglion cell, tuned to certain spatio-temporal features of the visual input, and its neural
238 population covers the entire visual field. How these parallel signals are combined and elaborated in
239 subsequent neural stages of the visual system to sustain the behavioral needs of the animal remains a
240 fundamental question for vision science. Here we sought to follow these parallel pathways into the
241 superior colliculus, the most important retinal projection target in rodents, which receives input from
242 ~90% of the retinal ganglion cells. The approach was to survey visual response properties across
243 many neurons in the superficial layers of the superior colliculus, using precisely those stimuli that
244 had been instrumental in defining the parallel pathways at the retinal output.

245 3.1 Main findings

246 Based on their responses to a broad set of visual stimuli, neurons in the upper SC fall into 24
247 functional types (Figures 2 and 3). At a coarse level, the types form two groups, depending on
248 whether they respond well to simple chirp stimuli (Group 1) or not (Group 2) (Figure 2A). Cells in
249 Group 1 dominate the most superficial regions (<100 um depth), those in Group 2 the deeper levels
250 (Figure 4H). Unlike in the retina – where cells of the same type are spaced laterally at a regular
251 distance – in the SC cells of the same type seem to attract each other. In fact many types appear in
252 clusters, about 300-500 μm in size (Figure 4). Putative excitatory and inhibitory neurons differ in
253 functional properties: On average the inhibitory neurons have a greater preference for large stimuli
254 and for stimulus motion (Figure 5). Compared to retinal ganglion cells, none of the SC types match
255 an RGC type exactly; instead different retinal sensitivities get combined at the level of SC (Figure 6).
256 Overall, the visual representation in the superficial SC is somewhat less diverse than in the retina
257 (Figure 6D).

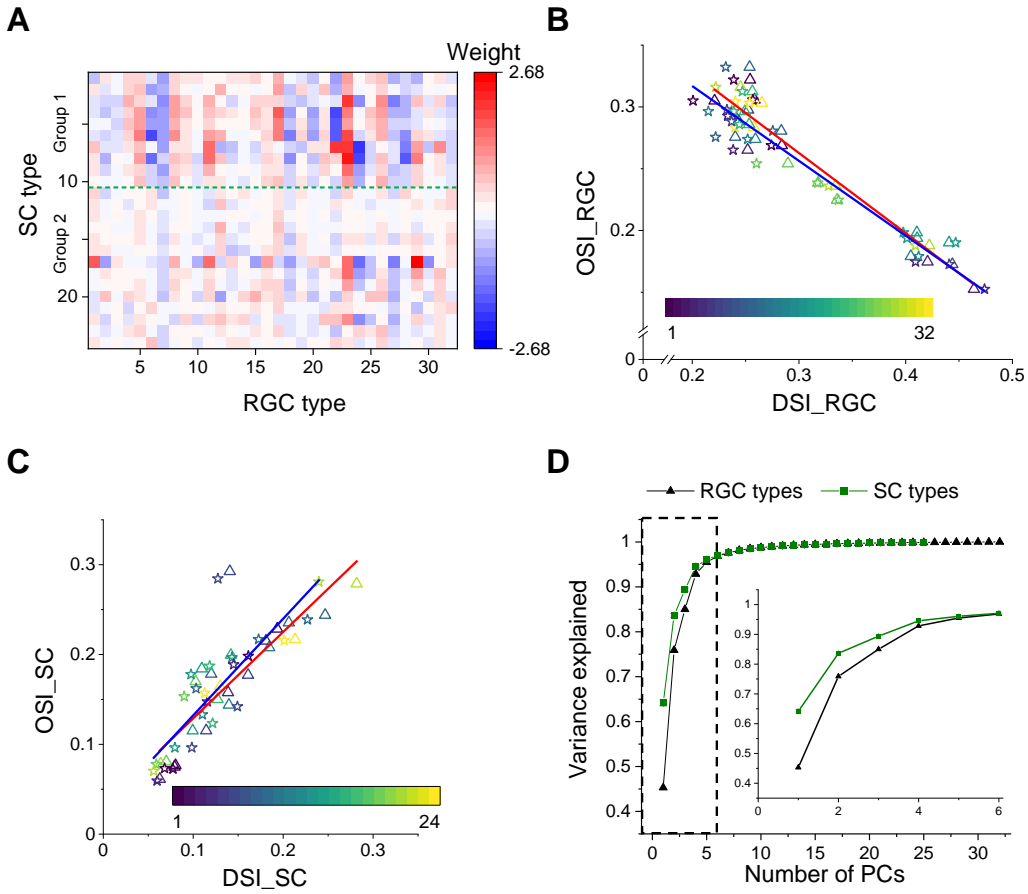


Figure 6: Comparison with functional RGC types. **A.** Weights of different RGC types on each SC type (see Methods). Green dashed line separates Group 1 and Group 2. **B.** Plot of mean (triangle) and median (star) OSI versus DSI for 32 functional RGC types. Data are from Baden et al. (2016). Color codes functional type. **C.** Plot of mean (triangle) and median (star) OSI versus DSI for 24 functional types in the SC. Color codes functional type. **D.** PCA of the visual responses of SC and RGC types, plotting the fractional explained variance against the number of components. Inset enlarges the part in the dashed rectangle. The uncertainty in these values was <0.01 (SD) in all cases, as estimated from a bootstrap analysis.

258 3.2 Relation to prior work

259 Although the superior colliculus receives many parallel channels of input from the retina and the
 260 visual cortex, prior work classified only 4-5 types of neurons in the SC (Wang et al., 2010; Gale and
 261 Murphy, 2014; De Franceschi and Solomon, 2018). The greater diversity of response types in the
 262 present study results in part from a different conceptual approach: Instead of defining cell types based
 263 on a combination of morphological, electrophysiological, and functional criteria (Wang et al., 2010;
 264 Gale and Murphy, 2014), we focused on visual response properties. This method acknowledges that
 265 neurons with the same shape do not necessarily perform the same function in the circuit. Indeed prior
 266 work had found that even among Ntsr1+ neurons that have distinctive wide-field shape there is a great
 267 range of response properties (Hoy et al., 2019).

268 Another supporting factor is the much greater number of neurons in the present survey, which allows
 269 finer distinctions and statistical assessment of robustness of the functional cell typing. Further, much
 270 of the prior work was conducted under anesthesia. This has adverse effects on visual selectivity in
 271 the superior colliculus, as pointed out by De Franceschi and Solomon (2018), and thus lowers the
 272 number of distinguishable cell types.

273 At the same time, some of the 24 functional types described here are also evident in prior studies:
274 Types 11 and 15 that show rebounded responses after the frequency-modulated flash are similar
275 to the suppressed-by-contrast cell type (Ito et al., 2017). Types 9 and 14 show strong orientation
276 and direction selectivity, as reported in prior work (Inayat et al., 2015; De Franceschi and Solomon,
277 2018).

278 The notion of dividing SC types into two groups is supported by a recent report (Sibille et al.,
279 2022). From simultaneous recordings of RGC axons and SC neurons, this study showed that one
280 group of SC neurons receives synaptic inputs from functionally homogeneous RGCs while another
281 group combines more functionally diverse inputs. Clearly this is a powerful way of assessing direct
282 retino-geniculate synapses. By contrast, our analysis includes indirect effects through interneuron
283 circuitry, and suggests that most SC neurons end up combining signals from multiple retinal channels
284 (Figure 6A).

285 3.3 Implications for visual processing

286 Regarding the fate of parallel pathways emerging from the retina, one can contemplate two opposing
287 hypotheses: (1) Further divergence of pathways. In this picture downstream circuits split the visual
288 representation further, yielding more functional types of neurons. Each type responds sparsely only
289 when its favorite feature occurs. (2) Convergence of parallel pathways. In this version downstream
290 circuits begin to narrow the visual representation, computing a few variables from the scene that are
291 useful for controlling behavior, while discarding those bits of information that aren't needed. The
292 present observations favor the second hypothesis, for the following reasons:

293 First, there are fewer recognizable types in this survey of SC responses (24) than there are in the retinal
294 ganglion cell layer (40) under the same tests. Some comments are in order regarding this comparison.
295 In the retina, the number of RGC types is supported by a convergence of functional, molecular, and
296 anatomical criteria (Sanes and Masland, 2015), leaving little ambiguity. By comparison, the proposed
297 number of 24 functional types in SC is open to debate. The statistical criterion we used (Figure 2b)
298 is not the only option, and one can envision a coarser split into fewer types. Furthermore, the cell
299 types reported here, as well as those in previous studies (Wang et al., 2010; Gale and Murphy, 2014;
300 De Franceschi and Solomon, 2018), may well lie at different levels of the synaptic network, whereas
301 the RGCs all lie in the same network layer of parallel representation. All these biases point in the
302 same direction: There are very likely fewer SC types than RGC types. Second, certain features of
303 the visual stimulus that were separated into different retinal cell types appear combined within the
304 superior colliculus. Notably this is the case for the representation of orientation and motion direction
305 (Figure 6C) and for that of On- and Off-signals (Figure 2A). Third, a global measure of dimensionality
306 in the neural representation is smaller among SC types than RGC types (Figure 6D). Note that ~10%
307 of RGCs avoid the SC, including SPIG1+ cells in the pan-ventronasal retina (Yonehara et al., 2008),
308 which could contribute to the reduction of dimensionality.

309 All this suggests that the functional diversity in the visual pathway may be greatest at the retinal
310 output. Subsequent circuits may act primarily as a switchboard to distribute these RGC signals to
311 different brain targets. For example, a recent study traced the projections from SC to two different
312 target areas, and found that the corresponding SC cells combine inputs from different subsets of retinal
313 ganglion cells (Reinhard et al., 2019). It will be interesting to explore how these projection-defined
314 types correspond to the functional types reported here and their putative RGC complements (Figure
315 6A).

316 Another output target from the superficial SC are the deeper layers, where visual information is
317 combined with other sensory pathways as well as motor signals. These are out of reach for effective
318 optical recording but can be accessed by electrodes. There one encounters response properties
319 not seen in the retina, foremost among them a pronounced habituation to repeated stimuli (Dräger
320 and Hubel, 1975; Horn and Hill, 1966; Lee et al., 2020). Also, the range of response properties
321 narrows systematically with depth, reflecting an increased selectivity for behaviorally-relevant visual
322 features (Lee et al., 2020). Similarly, it is possible that the functional types varies across regions
323 of the SC. Stimulating the region that represents the upper or low visual field elicits avoidance or
324 orientating behavior respectively (Sahibzada et al., 1986), suggesting that other functional types
325 relevant to orienting behaviors likely exist in regions outside the posterior medial sector studied here.

326 **3.4 The spatial organization of functional cell types**

327 The patchy organization of functional cell types (Figure 4) extends the results reported previously
328 regarding specific neuronal response properties, notably the preferred orientation (Feinberg and
329 Meister, 2015; Ahmadlou and Heimel, 2015; Sibille et al., 2022) or movement direction (Li et al.,
330 2020; de Malmazet et al., 2018). A common theme to all these reports is that the rules of visual
331 processing seem to vary across broad regions of the visual field (for a dissenting report see Chen et al.
332 (2021)). In the present study we found that different regions of the visual field, measuring ~20-40
333 degrees across, are covered by a different complement of functional types. Our recordings were
334 limited to the posterior-medial portion of the SC (upper temporal visual field), and thus the global
335 organization of these functional types remains unclear. Also, it is possible that additional functional
336 types will emerge in other parts of the visual field.

337 It is important to contrast this organization with inhomogeneities found elsewhere in the visual system.
338 Among retinal ganglion cells (RGCs), the mosaic arrangement of neurons within a type guarantees
339 that they are properly spaced, such that each point in the visual field is handled by at least one such
340 ganglion cell. Within a given RGC type, the response properties may vary gradually across the visual
341 field, typically in a naso-temporal or dorso-ventral gradient (Bleckert et al., 2014; Warwick et al.,
342 2018). This is very different from the regional specializations encountered in the SC. In the primary
343 visual cortex of large animals one often finds that functional types are organized in patches or stripes.
344 However, the scale of this functional anatomy is finer than the receptive field size: This guarantees
345 again that each point in the visual field is handled by neurons of every type (Blasdel and Campbell,
346 2001). By contrast, in the SC the observed patches are 10-20 times larger than receptive fields,
347 which implies a regional specialization of certain visual processes. The reasons for this specialization
348 remain unclear. One can certainly invoke ecological arguments for treating the upper and lower visual
349 fields differently, but on the scale of 30 degrees the purpose is less obvious.

350 Future work may also inspect the downstream effects of this patchy organization. One hypothesis is
351 that a given functional type gathers visual information for distribution to one of the many downstream
352 visual centers. If so, then a retrograde tracing from one of the SC's target regions should cover only a
353 patch of the visual field. The rapid progress in connectomic and transcriptomic methods for mapping
354 cell types promises further insights into this unusual functional organization.

355 **4 Materials and Methods**

356 **4.1 Animal**

357 Laboratory mice of both sexes were used at age 2–4 months. The strains were C57BL/6J
358 (wild-type), Vglut2-ires-Cre (B6J.129S6(FVB)-*Slc17a6*^{tm2(cre)LowL}/MwarJ, JAX: 028863), Vgat-
359 ires-Cre (B6J.129S6(FVB)-*Slc32a1*^{tm2(cre)LowL}/MwarJ, JAX: 028862), Tac1-IRES2-Cre-D (B6;129S-
360 *Tac1*^{tm1.1(cre)Hze}/J, JAX: 021877) (Harris et al., 2014), Rorb-IRES2-Cre-D (B6;129S-*Rorb*^{tm1.1(cre)Hze}/J,
361 JAX: 023526) (Harris et al., 2014), and Ntsr1-GN209-Cre (Genset: 030780-UCD) (Gerfen et al.,
362 2013). Vglut2-ires-Cre and Vgat-ires-Cre mice express Cre recombinase in *Vglut2*-expressing and
363 *Vgat*-expressing neurons respectively. Tac1-IRES2-Cre-D and Rorb-IRES2-Cre-D mice express
364 Cre recombinase in *Tac1*-expressing and *Rorb*-expressing neurons respectively. Cre-D indicates
365 neo/hydro is deleted. Ntsr1-GN209-Cre mice express Cre recombinase in *Ntsr1*-GN209-expressing
366 neurons. GN209 is the founder line. All animal procedures were performed according to relevant
367 guidelines and approved by the Caltech IACUC.

368 **4.2 Viral injection**

369 We injected adeno-associated virus (AAV) expressing non-floxed GCaMP6
370 (AAV2/1.hSyn1.GCaMP6f.WPRE.SV40) into the SC of wild-type mice (C57BL/6J), and
371 AAV expressing floxed GCaMP6 (AAV1.Syn.Flex.GCaMP6f.WPRE.SV40) into the SC of
372 Vglut2-ires-Cre, Vgat-ires-Cre, Tac1-IRES2-Cre-D, Rorb-IRES2-Cre-D, and Ntsr1-GN209-Cre
373 mice. After 2–3 weeks, we implanted a cranial window coupled to a transparent silicone plug that
374 rested on the surface of the SC and exposed its posterior-medial portion. This portion of the SC
375 corresponds to the upper-temporal part of the visual field. The optics remained clear for several
376 months, which enabled long-term monitoring of the same neurons. Two-photon microscopy was
377 used to image calcium signals in the SC of head-fixed awake mice 3 weeks to 2 months after viral
378 injection.

379 **4.3 In vivo two-photon calcium imaging**

380 For imaging experiments, the animal was fitted with a head bar, and head-fixed while resting on
381 a rotating treadmill. The animal was awake and free to move on the treadmill, but not engaged in
382 any conditioned behavior. Two-photon imaging was performed on a custom-built microscope with
383 a 16×, 0.8 NA, 3 mm WD objective (Nikon). A Ti:Sapphire laser with mode-locking technique
384 (Spectra-Physics Mai Tai HP DeepSee) was scanned by galvanometers (Cambridge). GCaMP6f was
385 excited at 920 nm and laser power at the sample plane was typically 20–80 mW. A 600 μm × 600
386 μm field of view was scanned at 4.8 Hz as a series of 250 pixel × 250 pixel images and the imaging
387 depth was up to 350 μm. Emitted light was collected with a T600/200dcrb dichroic (Chroma), passed
388 through a HQ575/250m-2p bandpass filter (Chroma), and detected by a photomultiplier tube (R3896,
389 Hamamatsu). Artifacts of the strobed stimulus (see below) were eliminated by discarding 8 pixels
390 on either end of each line. The animal’s locomotion on the treadmill and its pupil positions were
391 recorded and synchronized to the image acquisition. The head-fixed animal performs only rare eye
392 movements and locomotion (Li et al., 2020).

393 **4.4 Visual stimulation**

394 An LCD screen with LED backlight was placed 18 cm away from the mouse’s right eye. The center
395 of the monitor was at 95° azimuth and 25° elevation in the laboratory frame, and the monitor covered
396 a visual field of 106° × 79°. The visual angle that covers the receptive fields of recorded neurons is
397 60°–140° azimuth and 0°–50° elevation (Figure 12). The monitor’s LED illuminator was strobed for
398 12 μs at the end of each laser scan line to minimize interference of the stimulus with fluorescence
399 detection. The monitor was gamma-corrected. For measuring the functional properties, we presented
400 six types of visual stimuli. (1) A full-field moving black bar (5° width at 50°/s) in 12 directions
401 to measure the orientation selectivity and direction selectivity. The sequence of directions was
402 pseudo-randomized. (2) An expanding black disc (diameter 2° to 60° at a speed of 60°/s, stationary
403 at 60° for 0.25 s, followed by grey background for 2 s) and a receding white disc (60° to 2° at a
404 speed of 60°/s, other parameters same as expanding disc) to measure looming-related responses. (3)
405 Sparse (one at a time) 5° × 5° flashing squares (11×11 squares, 1 s black or white + 1 s grey) to map

406 the receptive field (RF); (4) A $10^\circ \times 10^\circ$ square modulated by a "chirp" in frequency or amplitude
 407 (3 s black + 3 s white + 3 s black + 3 s grey + 8 s frequency modulation ($2^{-1.3}$ Hz) + 3 s grey +
 408 8 s amplitude modulation (0 : 1) + 3 s grey + 3 s black) centered on the RF to measure temporal
 409 properties (Baden et al., 2016); (5) A $10^\circ \times 10^\circ$ square flashing blue or green (1 s black + 3 s blue +
 410 4 s black + 3 s green + 3 s black) centered on the RF to measure the color preference; (6) A flashing
 411 disc (2 s black + 2 s grey) with different size ($2^\circ, 4^\circ, 8^\circ, 16^\circ, 32^\circ$) centered on the RF to measure
 412 the size tuning. All stimuli were displayed for 10 repetitions. Stimuli of types 4, 5, and 6 were also
 413 repeated identically at locations in a 3×3 array shifted by 10° . This effectively covered the visual
 414 field recorded during a given imaging session. For each neuron, we based the analysis on the stimulus
 415 closest to its receptive field center.

416 4.5 Analysis of calcium responses

417 4.5.1 Measurement of calcium responses

418 Brain motion during imaging was corrected using SIMA (Kaifosh et al., 2014) or NoRMCorre (Pnev-
 419 matikakis and Giovannucci, 2017). Regions of interest (ROIs) were drawn manually using Cell
 420 Magic Wand Tool (ImageJ) and fitted with an ellipse in MATLAB. Fluorescence traces of each ROI
 421 were extracted after estimating and removing contamination from surrounding neuropil signals as
 422 described previously (Feinberg and Meister, 2015; Li et al., 2020; Göbel and Helmchen, 2007; Kerlin
 423 et al., 2010). The true fluorescence signal of a neuron is $F_{\text{true}} = F_{\text{raw}} - (r \cdot F_{\text{neuropil}})$, where r is
 424 the out-of-focus neuropil contamination factor and the estimated value for our setup is ~ 0.7 . Slow
 425 baseline fluctuations were removed by subtracting the eighth percentile value from a 15 s window
 426 centered on each frame (Dombeck et al., 2007).

427 For any given stimulus, the response of a neuron was defined by the fluorescence trace in its ROI
 428 during the stimulus period:

$$R = \frac{F - F_0}{F_0} \quad (1)$$

429 where F is the instantaneous fluorescence intensity and F_0 is the mean fluorescence intensity without
 430 visual stimulation (grey screen).

431 Two criteria were applied to interpret ROIs as neurons: 1) The size of the ROI was limited to 10-20
 432 μm to match the size of a neuron; 2) The response from the ROI had to pass a signal-to-noise ratio
 433 (SNR) of 0.35 (Baden et al., 2016),

$$SNR = \frac{\text{Var}[\langle C \rangle_r]_t}{\langle \text{Var}[C]_r \rangle_t} \quad (2)$$

434 where C is the N_t (time samples) $\times N_r$ (stimulus repetitions) response matrix, $t = 1, \dots, N_t$ and
 435 $r = 1, \dots, N_r$, $\langle \cdot \rangle_r$ and $\langle \cdot \rangle_t$ are the means over repetitions or time respectively, and $\text{Var}[\cdot]_r$ and
 436 $\text{Var}[\cdot]_t$ are the corresponding variances. All ROIs meeting these criteria were selected for further
 437 analysis, yielding a total of 3414 neurons, including 490 neurons from four wild type mice, 337
 438 neurons from one Vglut2-ires-Cre mouse, 1085 neurons from three Vgat-ires-Cre mice, 720 neurons
 439 from three Tac1-IRES2-Cre-D mice, 485 neurons from four Rorb-IRES2-Cre-D mice, and 297
 440 neurons from one Ntsr1-GN209-Cre mouse.

441 4.5.2 Quantification of functional properties

442 The functional properties introduced in Figure 3 are defined as follows:

443 The response to motion (RtM) is the response value during moving-bar stimuli with the largest
 444 absolute value. For neurons suppressed by motion this will be negative.

445 To quantify the tuning of a neuron to motion directions, we calculated the direction selectivity index
 446 (DSI) as the normalized amplitude of the response-weighted vector sum of all directions:

$$DSI = \frac{|\sum_k R(\rho_k) \times e^{i\rho_k}|}{\sum_k R(\rho_k)} \quad (3)$$

447 Where ρ_k is the k^{th} direction in radians and $R(\rho_k)$ is the peak response at that direction.

448 To quantify the orientation tuning, we calculated the orientation selectivity index (OSI) as the
449 normalized amplitude of the response-weighted vector sum of all orientations:

$$OSI = \frac{|\sum_k R(\theta_k) \times e^{2i\theta_k}|}{\sum_k R(\theta_k)} \quad (4)$$

450 Where θ_k is the k^{th} orientation in radians and $R(\theta_k)$ is the peak response at that orientation.

451 To quantify the habituation to the expanding black disc, we calculated the habituation index (HI):

$$HI = \frac{R_1 - R_{10}}{R_1 + R_{10}} \quad (5)$$

452 where R_1 and R_{10} are the peak response to the first and the tenth looming stimulus respectively.

453 To quantify the selectivity to the expanding black disc over the receding white disc, we calculated the
454 looming selectivity index (LSI):

$$LSI = \frac{R_k - R_w}{R_k + R_w} \quad (6)$$

455 where R_k is the peak response to the black expanding disc and R_w is the peak response to the white
456 receding disc.

457 To quantify the selectivity to moving stimuli over the flashing stimuli, we calculated the motion
458 selectivity index (MSI):

$$MSI = \frac{R_m - R_f}{R_m + R_f} \quad (7)$$

459 where R_m is the peak response to the moving bar at the preferred direction and R_f is the peak
460 response to the flashing chirp stimulus.

461 To quantify the selectivity to On/Off contrast, we calculated the contrast selectivity index (CSI):

$$CSI = \frac{R_{On} - R_{Off}}{R_{On} + R_{Off}} \quad (8)$$

462 where R_{On} is the peak response to the flashing white square and R_{Off} is the peak response to the
463 flashing black square.

464 To quantify whether neurons show transient or sustained responses to flash stimuli, we calculated the
465 peak-final selectivity index (PFSI):

$$PFSI = \frac{R_{peak} - R_{final}}{R_{peak} + R_{final}} \quad (9)$$

466 where R_{peak} is the peak response to the flashing white/black square that elicited larger responses,
467 and R_{final} is the final response to that stimulus.

468 To quantify the selectivity to the flash frequency, we calculated the frequency selectivity index (FSI):

$$FSI = \frac{R_{low} - R_{high}}{R_{low} + R_{high}} \quad (10)$$

469 where R_{low} is the peak response in the first 3 seconds to the flashing frequency modulation, and
470 R_{high} is the peak response in the last 2 seconds to the frequency modulation.

471 We measured the response after frequency modulation (RaFM) as the difference between the response
472 amplitude at 1.6 s after the stop of the frequency modulation and the baseline. Similarly, the response

- 473 after amplitude modulation (RaAM) was measured as the difference between the response amplitude
 474 at 1.6 s after the stop of the amplitude modulation and the baseline.
 475 The best stimulation size (BSS) was defined the size of flashing black disc that elicited the largest
 476 responses.
 477 To quantify the surround suppression, we calculated the surround suppression index (SSI):

$$SSI = \frac{R_{\text{small}} - R_{\text{large}}}{R_{\text{small}} + R_{\text{large}}} \quad (11)$$

- 478 where R_{small} is the peak response to the flashing black disc with a diameter of 2 degrees, and R_{large}
 479 is the peak response to the flashing black disc with a diameter of 32 degrees.
 480 To quantify the color preference, we calculated the blue-green index (BGI):

$$BGI = \frac{R_b - R_g}{R_b + R_g} \quad (12)$$

- 481 where R_b is the response to the flashing blue stimulus and R_g is the response to the flashing green
 482 stimulus.
 483 To quantify the receptive field size (RFS), the calcium responses at 11×11 locations were fitted with
 484 a 2-D Gaussian function (Equation 13),

$$f = A \cdot e^{-\frac{((x-E)\cos(D)-(y-F)\sin(D))^2}{2B^2} - \frac{((x-E)\sin(D)+(y-F)\cos(D))^2}{2C^2}} + G \quad (13)$$

- 485 The RF size is defined as the area at the tenth of maximum, which equals $\pi \cdot 2 \ln 10 \cdot B \cdot C$. We
 486 omitted analysis of the RF if the coefficient of determination for this fit was below 0.5 (Figure 10C).
 487 The RF size of neurons with the coefficient of determination larger than 0.5 is shown in Figures 3-5.

488 4.5.3 Construction of the feature matrix

- 489 We reduced the dimensionality of the calcium response traces, by approximating them with a weighted
 490 sum of features, while requiring that the weight coefficients be sparse. For this analysis we included
 491 the neuronal responses to moving bars (MB), expanding black and receding white disc (EBD and
 492 RWD), chirp, color, flashed black discs with different sizes (FDDS). Neuronal responses to MB,
 493 EBD, and RWD were aligned to the peak or the trough to remove the effect of RF position. We
 494 focused on neurons which responded robustly ($\text{SNR} > 0.35$) to at least one stimulus. For each neuron
 495 and each stimulus, the response was normalized to $[0, 1]$. The optimal features were extracted with
 496 sparse principal components analysis (spca) (Mairal et al., 2009), as implemented in the scikit-learn
 497 package (equation 14).

$$\mathbf{D} = \mathbf{X}\mathbf{F} \quad (14)$$

- 498 where \mathbf{D} ($N_{\text{neuron}} \times N_{\text{time}}$) is the data matrix denoting neuronal responses to a visual stimulus,
 499 \mathbf{F} ($N_{\text{feature}} \times N_{\text{time}}$) is the matrix with the time course corresponding to each feature, and \mathbf{X} ($N_{\text{neuron}} \times$
 500 N_{feature}) is the matrix of weight coefficients. \mathbf{F} is regularized so that only sparse values in each row
 501 are non-zero, and $\mathbf{FF}^\top \approx \mathbf{I}$.

- 502 We extracted 6 features from the responses to MB at the preferred direction, 6 features from the
 503 responses to EBD and RWD, 20 features from the chirp, 8 features from color stimuli, and 10 features
 504 from FDDS (Figure 7A). These extracted features were combined with HI, DSI, OSI, and MSI to
 505 make the feature matrix. Each feature was normalized so that the mean is 0 and the standard deviation
 506 is 1.

507 **4.5.4 Clustering of the feature matrix**

508 We used a Gaussian mixture model (GMM) to fit the distribution of neurons in the space of features.

$$p(x) = \sum_{i=1}^K \phi_i N(x|\mu_i, \sigma_i) \quad (15)$$

$$N(x|\mu_i, \sigma_i) = \frac{1}{\sigma_i \sqrt{2\pi}} \exp\left(-\frac{(x - \mu_i)^2}{2\sigma_i^2}\right) \quad (16)$$

$$\sum_{i=1}^K \phi_i = 1 \quad (17)$$

509 where $p(x)$ is the probability density of the feature vector x , K is the number of component Gaussian
 510 functions, and ϕ_i is the weight for i^{th} Gaussian function $N(x|\mu_i, \sigma_i)$ in the feature space. We
 511 optimized the parameters using the EM algorithm (sklearn.mixture.GaussianMixture in the package
 512 scikit-learn). We varied the number of components from 2 to 50 and evaluated the quality with the
 513 Bayesian information criterion (BIC) (Kass and Raftery, 1995):

$$BIC = -2 \ln L + k \ln n \quad (18)$$

514 where $L = p(x|\theta, M)$, is the maximized likelihood of model M , x is the observed data, θ are the
 515 parameters that maximize the likelihood, k is the number of parameters in the model, n is the number
 516 of neurons. For each putative number of components (2 to 50), we performed the EM fit starting
 517 from 1000 random initial states, and chose the fit with the smallest BIC. This minimal BIC is plotted
 518 against the number of components in Figure 2B.

519 To evaluate the stability of clusters, we applied sub-sampling analysis (Hennig, 2007). We randomly
 520 sub-sampled 90% of the dataset 1000 times and fitted the subset with a GMM using the best cluster
 521 number determined from the full dataset. For each original cluster, we calculated its Jaccard similarity
 522 coefficient (JSC) with the subsets,

$$JSC = \frac{1}{N} \sum_{i=1}^N \max_j \left\{ \frac{|C_{\text{full}} \cup C_{\text{sub}}^j|}{|C_{\text{full}} \cap C_{\text{sub}}^j|} \right\} \quad (19)$$

523 where N is the number of subsets, C_{full} is the cluster in the full dataset, and C_{sub}^j is the j^{th} cluster in
 524 one subset. Clusters with JSC below 0.5 were considered unstable. The unstable cluster was merged
 525 with the cluster that had the highest between-cluster rate if that rate was $> 35\%$ (Gouwens et al.,
 526 2019); otherwise, it was marked as unstable in the figure.

527 To assess the robustness of classification by the EM algorithm, we measured the probability that a
 528 pair of cells is classified into the same cluster in different subsets, and calculated the co-association
 529 matrix (Fred and Jain, 2005):

$$CAM(i, j) = \frac{n_{i,j}}{N} \quad (20)$$

530 where $n_{i,j}$ is the number of times that the pair (i, j) is assigned to the same cluster in N subsets. The
 531 between-cluster rate is defined as the cluster-wise average of the co-association matrix.

532 To plot the dendrogram, we applied a linkage algorithm (scipy.cluster.hierarchy.linkage) to the means
 533 of different clusters in the feature space. We measured the Euclidean distance between two points
 534 and defined the distance between two clusters with Ward's minimum variance method.

535 **4.5.5 Relative selectivity index**

536 Relative selectivity index (RSI) is defined as the difference of functional property between one type
 537 and a reference number.

$$RSI(i, j) = F_{i,j} - F_{i,ref} \quad (21)$$

538 where $F_{i,j}$ is functional property i of type j and $F_{i,ref}$ is the reference of functional property i .
 539 The functional properties are response to motion (RtM), motion selectivity index (MSI), direction
 540 selectivity index (DSI), orientation selectivity index (OSI), habituation index (HI), looming selectivity
 541 index (LSI), contrast selectivity index (CSI), peak-final selectivity index (PFSI), response after
 542 frequency modulation (RaFM), response after amplitude modulation (RaAM), best stimulation size
 543 (BSS), surround suppression index (SSI), blue-green selectivity index (BGSI), receptive field size
 544 (RFS). The reference numbers are RtM: 0, DSI: 0.15, OSI: 0.15, HI: 0, LSI: 0, MSI: 0, CSI: 0, PFSI:
 545 0.5, FSI: 0, RaFM: 0, BSS: 2^3 , SSI: 0, BGSI: 0, RFS: $10^{2.46}$.

546 **4.5.6 Analysis of the anatomical arrangement of functional cell types**

547 For the results on anatomical arrangement (Figure 4), only recording sessions with >5 neurons in a
 548 field of view were included. The density recovery profile (DRP) plots the probability per unit area
 549 of finding a cell as a function of distance from a cell of the same type (Rodieck, 1991). We first
 550 defined the region of interest (ROI) as the convex hull of all neurons in an image. Within this ROI,
 551 we measured the distances from each reference cell to all of the other cells and histogrammed those,
 552 which yields

$$N(r)\Delta r = \text{average number of cells at radii between } r \text{ and } r + \Delta r \quad (22)$$

553 Then we measured the average area $A(r)\Delta r$ at distance between r and $r + \Delta r$ from any reference
 554 point in the window.

555 Finally the DRP was calculated as

$$\rho(r) = \frac{N(r)}{A(r)} \quad (23)$$

556 The density ratio (DR) for each type is calculated as

$$DR(i) = \frac{\rho_i(r_0)}{\rho_i(r_1)} \quad (24)$$

557 where $\rho_i(r_0)$ is the mean density of functional type i within $0.5R$ of a cell of that type, R is the
 558 average receptive field diameter of that type, and $\rho_i(r_1)$ is the mean density in the annulus spanning
 559 $0.5 - 1R$. To connect anatomical distance in the SC with angular distance in the visual field we
 560 assumed that 1 mm corresponds to 88 degrees (Dräger and Hubel, 1976).

561 To quantify how the functional type of one neuron is related to the functional types of its neighbors,
 562 we calculated the density of different types

$$D(i, j) = \frac{n_{i,j}}{N_j} \quad (25)$$

563 where $n_{i,j}$ is number of neurons of functional type j within a certain distance to a neuron of type
 564 i , and N_j is the number of neurons of functional type j in the same area if neurons were uniformly
 565 distributed.

566 To quantify the relationship between two types of neurons, we calculated their normalized distance
 567 (ND) for each image

$$ND(i, j) = \frac{d_{i,j}}{0.5 \times (pd_i + pd_j)} \quad (26)$$

568 where $d_{i,j}$ is the Euclidean distance between the center of types i and j , and pd_i is the mean pairwise
569 distance between neurons of type i .

570 To quantify the significance of the separation between two types, we shuffled labels for all neurons in
571 these two clusters and calculated the p-value with bootstrap analysis to test whether the two types are
572 significantly separated. If the maximum p-value of all images that have ≥ 10 neurons for both types
573 is ≤ 0.01 , these two types are significantly separated.

574 **4.5.7 Retina-SC transformation**

575 For each type of SC neuron, we asked whether its responses can be explained by superposition of a
576 small number of retinal ganglion cell types (Fig 6A). Given the known responses of RGC types to
577 these same stimuli (Baden et al., 2016) we approximated the response of each SC type as a weighted
578 combination of RGC responses.

$$\arg \min_{\mathbf{a}} \|\mathbf{X}\mathbf{a} - \mathbf{y}\|_2 \quad (27)$$

579 where \mathbf{y} is the response vector of the SC type, \mathbf{X} is the matrix of the response vectors to the same
580 stimuli for all types of RGCs, and \mathbf{a} is the desired set of weights. The prediction error is quantified as

$$\frac{\|\mathbf{X}\mathbf{a} - \mathbf{y}\|_2}{\|\mathbf{y}\|_2} \quad (28)$$

581 **5 Supplement**

582 Here we report details related to the Results and Methods sections.

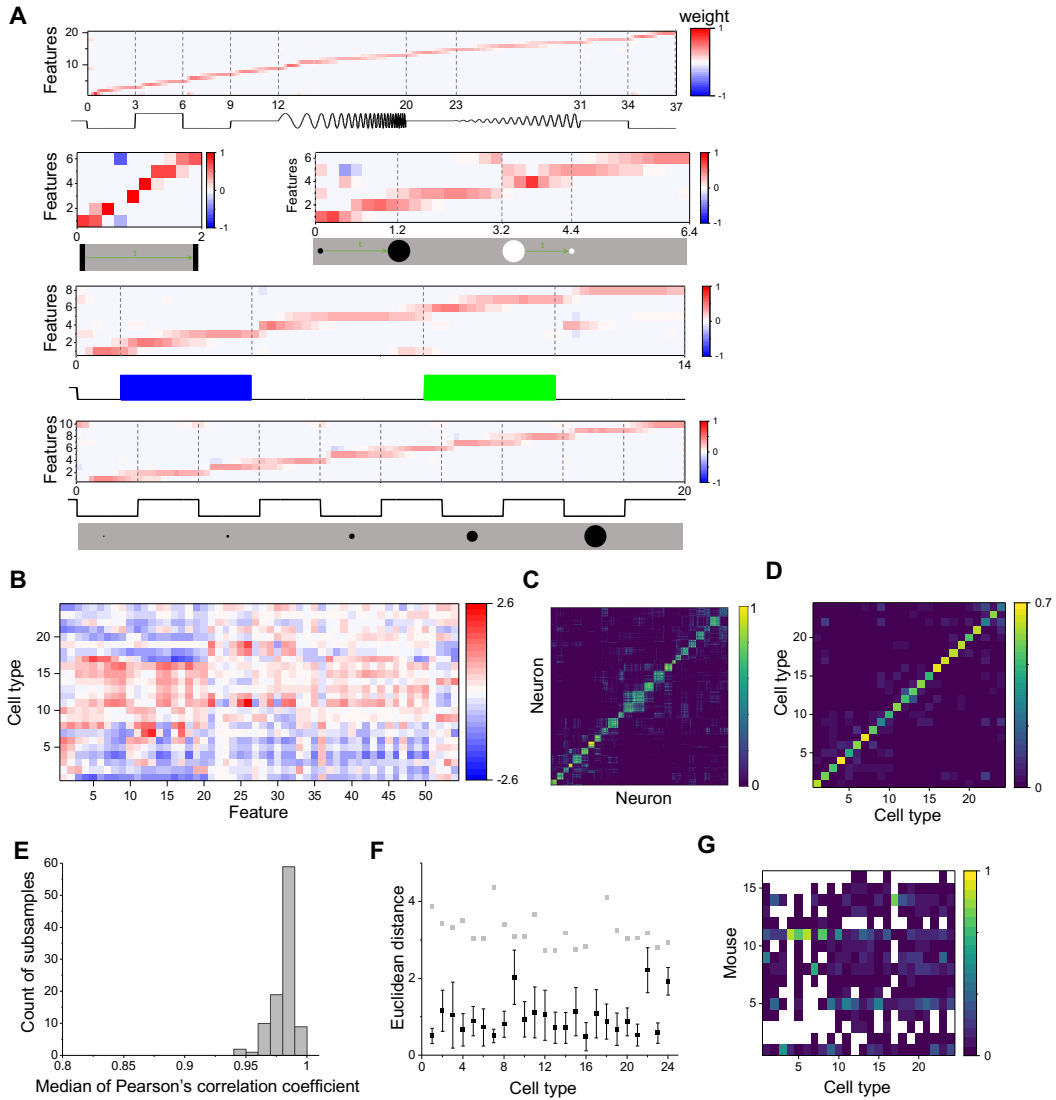


Figure 7: Clustering and validating (related to Figure 2). **A.** Temporal features were extracted from responses to five visual stimuli, including chirp, moving bar, expanding black disc and receding white disc, flashed blue or green squares, and flashed black discs with different sizes. Horizontal axis: time in s. **B.** Feature-coefficients for the 24 cell types. Color bar indicates coefficients of features for each cell type. **C.** Cell-wise co-association matrix (see Methods). Color bar indicates co-clustering fraction. **D.** Between-cluster rate, which is the cluster-wise average of the co-association matrix. **E.** Histogram of median correlation coefficients between the original clusters and clusters identified on 100 subsets. **F.** Black symbols indicate the Euclidean distance between original clusters and clusters identified on the subsets. Grey symbols indicate the shortest Euclidean distance between the original cluster and other clusters. **G.** Contributions of different mice to each of the functional types. White color indicates no contribution.

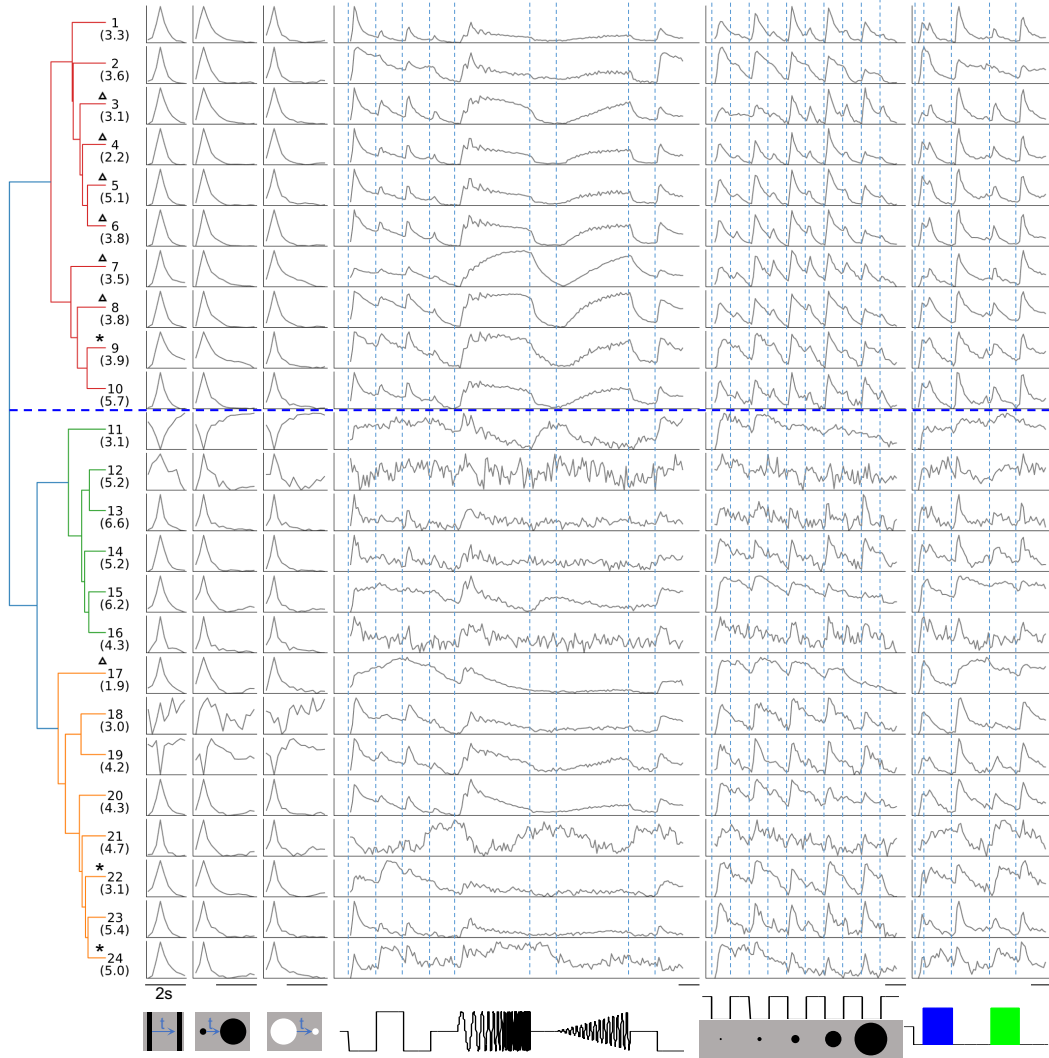


Figure 8: **Dendrogram of 24 clusters showing normalized temporal profiles (related to Figure 2).** Display as in Figure 2A. Blue dashed line separates groups 1 and 2. Numbers in parentheses indicate percentage of each type. Stars mark the unstable clusters with $JSC < 0.5$ (see Figure 2D). Triangles mark the clusters where more than half of the neurons are contributed by one mouse.

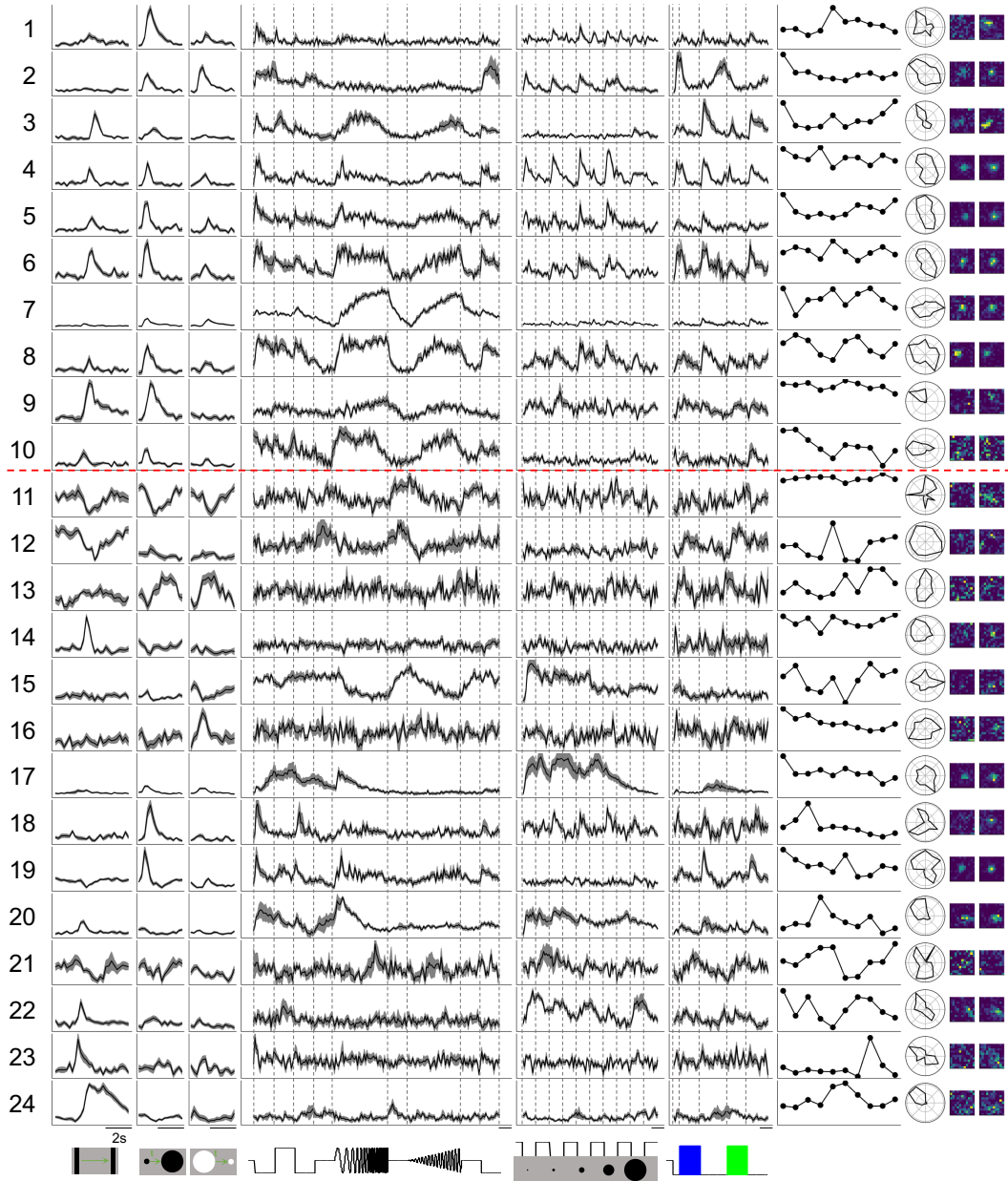


Figure 9: Example responses of single neurons in each type to visual stimuli (related to Figure 2). Columns 1-6 are time-varying calcium responses to a moving bar, expanding and contracting disks, a "chirp" stimulus with modulation of amplitude and frequency, spots of varying size, and blue and green flashes. Gray shading indicates the standard error across identical trials. Each row is scaled to the maximal response. Scale bars: 2 s. Subsequent columns show processed results: (7) response amplitude to an expanding black disc on 10 consecutive trials. (8) polar graph of response amplitude to moving bar in 12 directions. (9 and 10) Receptive field profiles mapped with small squares flashing On or Off. Red dashed line separates Group 1 and Group 2.

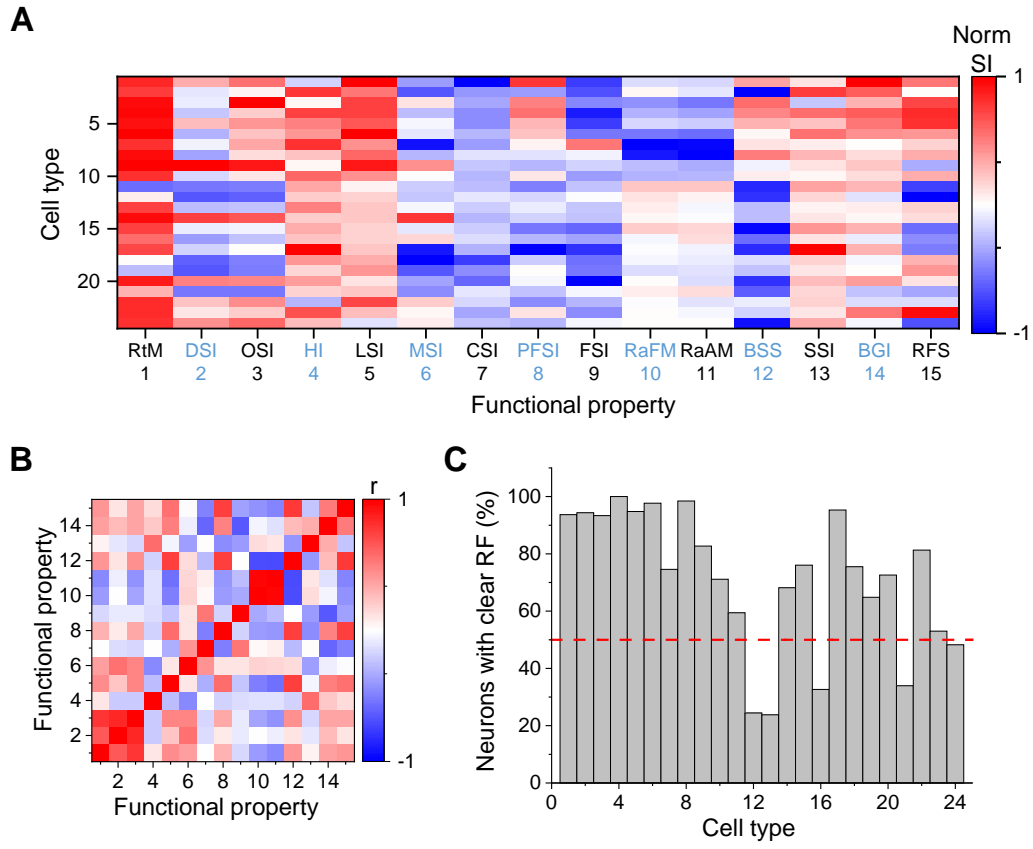


Figure 10: **Functional properties of different cell types (related to Figure 3).** **A.** Normalized selectivity index (normalized for each column) of functional properties represented by different cell types (see Methods). **B.** Pearson's correlation coefficients of the representation between pairs of functional properties. **C.** Percentage of neurons that show clear receptive fields to flash stimuli for each cell type.

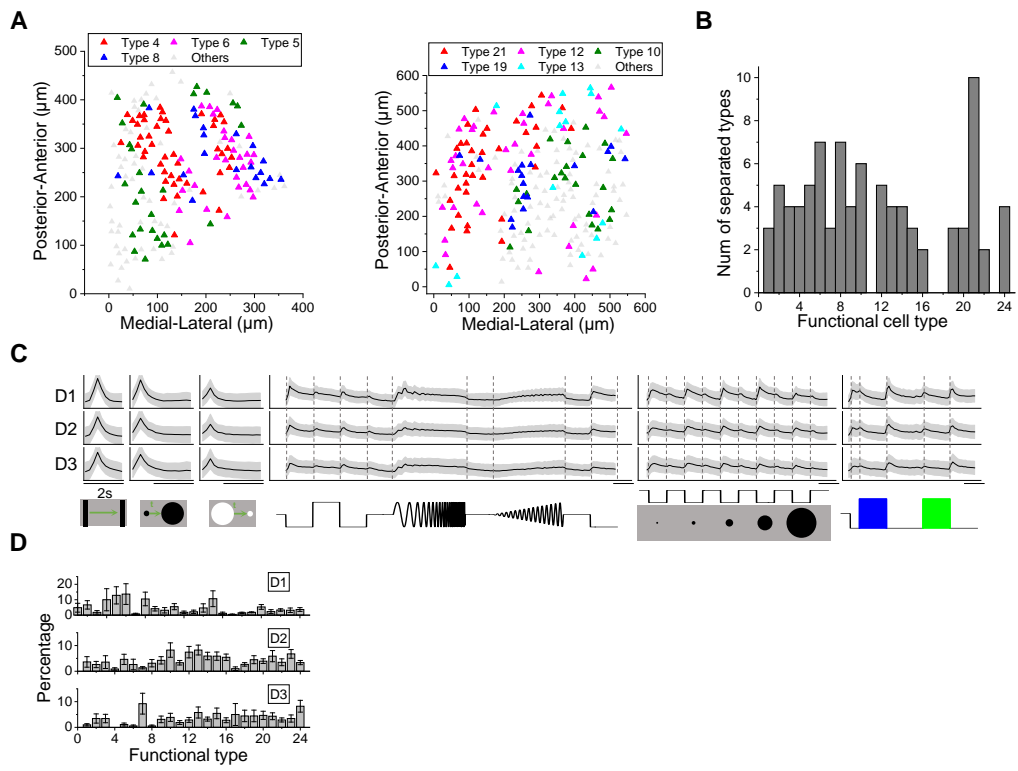


Figure 11: Anatomical organization of functional types (related to Figure 4). **A.** Anatomical locations of different types of neurons in two examples of imaging fields. **B.** Number of types that are significantly separated from each reference type ($p < 0.05$, bootstrap analysis). **C.** Temporal response across depth. Display as in Figure 2A. **D.** The percentage of functional cell types across depth. Error bars denote SEM.

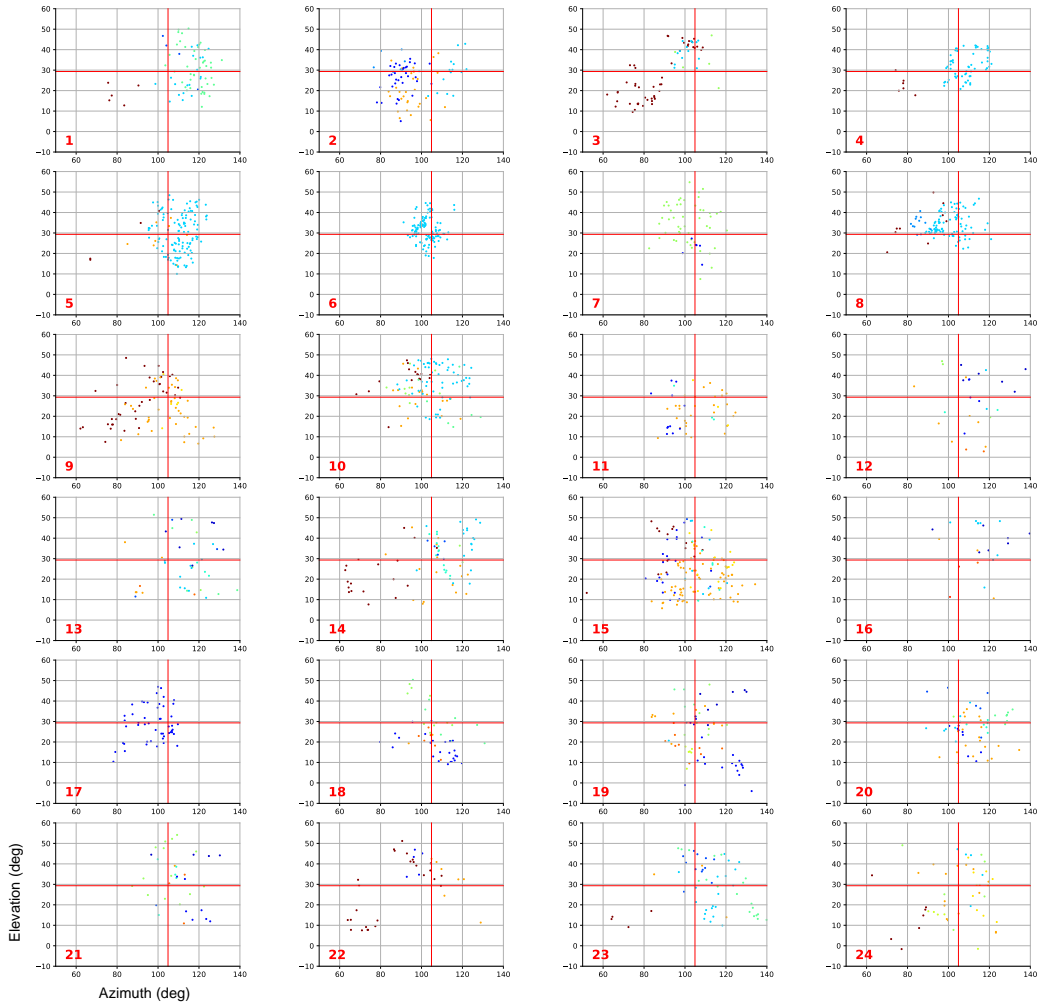


Figure 12: Receptive field center positions for each functional type (related to Figure 4). Cell types are indicated by the red number at the corner. Color indicates different mice. Axes represent azimuth (horizontal) and elevation (vertical) in degrees. Red cross indicates median azimuth and elevation for all types.

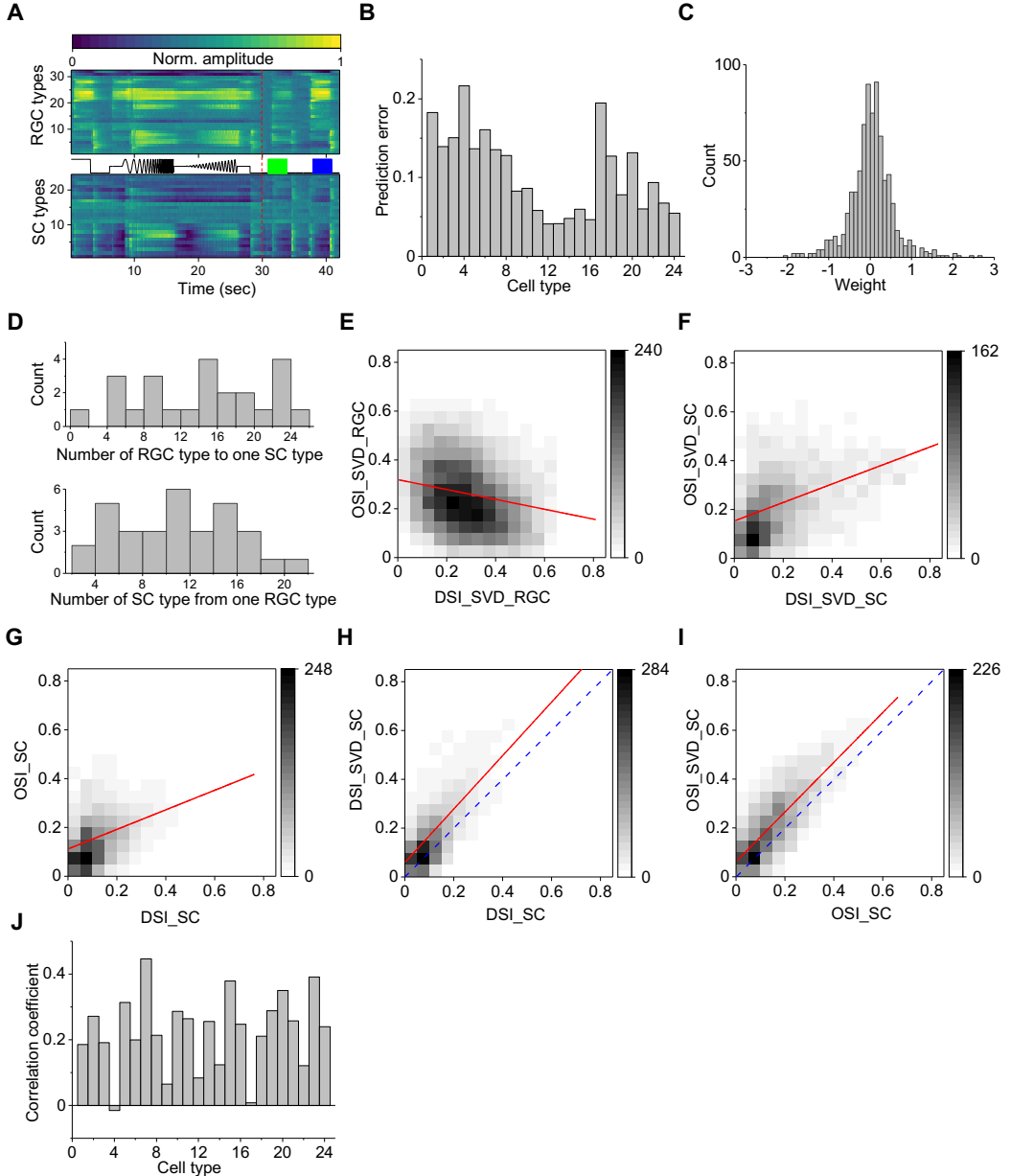


Figure 13: Comparisons between SC neurons and RGCs (related to Figure 6). **A.** Visual responses of RGC types (Baden et al., 2016) and SC types. **B.** Prediction error from RGC types to SC types (Eqn 28). **C.** Histogram of the weights of RGC types to SC types in Figure 6A. **D.** If one only considers weights $|w| > 0.3$, this histograms the number of RGC types contributing to one SC type, and vice versa the number of SC types with contributions from one RGC type. **E.** Plot of OSI vs DSI among RGCs, as reported in Baden et al. (2016). **F.** Plot of OSI vs DSI for SC neurons, calculated from the present study by the same SVD algorithm used in Baden et al. (2016). **G.** Plot of OSI vs DSI for SC neurons, using the simpler definition from the present study. **H.** Plot of DSI for SC neurons, computed by the SVD algorithm (Baden et al., 2016) versus the present definition. Note the close correspondence. **I.** As panel (H) for OSI. This analysis shows that the comparison between the retina results in Baden et al. (2016) and SC results in the present study does not suffer from different analysis methods. **J.** Correlation coefficients between OSI and DSI for each functional type.

583 **References**

- 584 Ahmadlou, M. and Heimel, J. A. (2015). Preference for concentric orientations in the mouse superior
585 colliculus. *Nature Communications*, 6:6773.
- 586 Baden, T., Berens, P., Franke, K., Román Rosón, M., Bethge, M., and Euler, T. (2016). The functional
587 diversity of retinal ganglion cells in the mouse. *Nature*, 529(7586):345–350.
- 588 Basso, M. A. and May, P. J. (2017). Circuits for Action and Cognition: A View from the Superior
589 Colliculus. *Annual Review of Vision Science*, 3(1):197–226.
- 590 Blasdel, G. and Campbell, D. (2001). Functional Retinotopy of Monkey Visual Cortex. *Journal of*
591 *Neuroscience*, 21(20):8286–8301.
- 592 Bleckert, A., Schwartz, G. W., Turner, M. H., Rieke, F., and Wong, R. O. L. (2014). Visual Space
593 Is Represented by Nonmatching Topographies of Distinct Mouse Retinal Ganglion Cell Types.
594 *Current Biology*, 24(3):310–315.
- 595 Byun, H., Kwon, S., Ahn, H.-J., Liu, H., Forrest, D., Demb, J. B., and Kim, I.-
596 J. (2016). Molecular features distinguish ten neuronal types in the mouse superficial
597 superior colliculus. *Journal of Comparative Neurology*, 524(11):2300–2321. _eprint:
598 <https://onlinelibrary.wiley.com/doi/10.1002/cne.23952>.
- 599 Chandrasekaran, A. R., Shah, R. D., and Crair, M. C. (2007). Developmental Homeostasis of Mouse
600 Retinocollicular Synapses. *Journal of Neuroscience*, 27(7):1746–1755.
- 601 Chen, H., Savier, E. L., DePiero, V. J., and Cang, J. (2021). Lack of Evidence for Stereotypical
602 Direction Columns in the Mouse Superior Colliculus. *Journal of Neuroscience*, 41(3):461–473.
603 Publisher: Society for Neuroscience Section: Research Articles.
- 604 De Franceschi, G. and Solomon, S. G. (2018). Visual response properties of neurons in the superficial
605 layers of the superior colliculus of awake mouse. *The Journal of Physiology*, 596(24):6307–6332.
- 606 de Malmazet, D., Kühn, N. K., and Farrow, K. (2018). Retinotopic Separation of Nasal and Temporal
607 Motion Selectivity in the Mouse Superior Colliculus. *Current Biology*, 28(18):2961–2969.e4.
- 608 Dombeck, D. A., Khabbaz, A. N., Collman, F., Adelman, T. L., and Tank, D. W. (2007). Imaging
609 Large-Scale Neural Activity with Cellular Resolution in Awake, Mobile Mice. *Neuron*, 56(1):43–
610 57.
- 611 Dräger, U. C. and Hubel, D. H. (1975). Responses to visual stimulation and relationship between vi-
612 sual, auditory, and somatosensory inputs in mouse superior colliculus. *Journal of Neurophysiology*,
613 38(3):690–713.
- 614 Dräger, U. C. and Hubel, D. H. (1976). Topography of visual and somatosensory projections to
615 mouse superior colliculus. *Journal of Neurophysiology*, 39(1):91–101.
- 616 Ellis, E. M., Gauvain, G., Sivy, B., and Murphy, G. J. (2016). Shared and Distinct Retinal Input to
617 the Mouse Superior Colliculus and Dorsal Lateral Geniculate Nucleus. *Journal of Neurophysiology*,
618 page jn.00227.2016.
- 619 Feinberg, E. H. and Meister, M. (2015). Orientation columns in the mouse superior colliculus. *Nature*,
620 519(7542):229–232.
- 621 Fred, A. L. N. and Jain, A. K. (2005). Combining multiple clusterings using evidence accumulation.
622 *IEEE Transactions on Pattern Analysis and Machine Intelligence*, 27(6):835–850. Conference
623 Name: IEEE Transactions on Pattern Analysis and Machine Intelligence.
- 624 Gale, S. D. and Murphy, G. J. (2014). Distinct Representation and Distribution of Visual Information
625 by Specific Cell Types in Mouse Superficial Superior Colliculus. *The Journal of Neuroscience*,
626 34(40):13458–13471.
- 627 Gale, S. D. and Murphy, G. J. (2016). Active Dendritic Properties and Local Inhibitory Input Enable
628 Selectivity for Object Motion in Mouse Superior Colliculus Neurons. *The Journal of Neuroscience*,
629 36(35):9111–9123.

- 630 Gale, S. D. and Murphy, G. J. (2018). Distinct cell types in the superficial superior colliculus project
631 to the dorsal lateral geniculate and lateral posterior thalamic nuclei. *Journal of Neurophysiology*,
632 120(3):1286–1292. Publisher: American Physiological Society.
- 633 Gerfen, C. R., Paletzki, R., and Heintz, N. (2013). GENSAT BAC Cre-Recombinase Driver Lines
634 to Study the Functional Organization of Cerebral Cortical and Basal Ganglia Circuits. *Neuron*,
635 80(6):1368–1383. Publisher: Elsevier.
- 636 Gouwens, N. W., Sorensen, S. A., Berg, J., Lee, C., Jarsky, T., Ting, J., Sunkin, S. M., Feng, D.,
637 Anastassiou, C. A., Barkan, E., Bickley, K., Blesie, N., Braun, T., Brouner, K., Budzillo, A.,
638 Caldejon, S., Casper, T., Castelli, D., Chong, P., Crichton, K., Cuhaciyan, C., Daigle, T. L., Dalley,
639 R., Dee, N., Desta, T., Ding, S.-L., Dingman, S., Doperałski, A., Dotson, N., Egdorf, T., Fisher,
640 M., Frates, R. A. d., Garren, E., Garwood, M., Gary, A., Gaudreault, N., Godfrey, K., Gorham,
641 M., Gu, H., Habel, C., Hadley, K., Harrington, J., Harris, J. A., Henry, A., Hill, D., Josephsen,
642 S., Kebede, S., Kim, L., Kroll, M., Lee, B., Lemon, T., Link, K. E., Liu, X., Long, B., Mann, R.,
643 McGraw, M., Mihalas, S., Mukora, A., Murphy, G. J., Ng, L., Ngo, K., Nguyen, T. N., Nicovich,
644 P. R., Oldre, A., Park, D., Parry, S., Perkins, J., Potekhina, L., Reid, D., Robertson, M., Sandman,
645 D., Schroedter, M., Slaughterbeck, C., Soler-Llavina, G., Sulc, J., Szafer, A., Tasic, B., Taskin,
646 N., Teeter, C., Thatra, N., Tung, H., Wakeman, W., Williams, G., Young, R., Zhou, Z., Farrell, C.,
647 Peng, H., Hawrylycz, M. J., Lein, E., Ng, L., Arkhipov, A., Bernard, A., Phillips, J. W., Zeng, H.,
648 and Koch, C. (2019). Classification of electrophysiological and morphological neuron types in the
649 mouse visual cortex. *Nature Neuroscience*, 22(7):1182–1195.
- 650 Göbel, W. and Helmchen, F. (2007). In Vivo Calcium Imaging of Neural Network Function.
651 *Physiology*, 22(6):358–365.
- 652 Harris, J. A., Hirokawa, K. E., Sorensen, S. A., Gu, H., Mills, M., Ng, L. L., Bohn, P., Mortrud, M.,
653 Ouellette, B., Kidney, J., Smith, K. A., Dang, C., Sunkin, S., Bernard, A., Oh, S. W., Madisen, L.,
654 and Zeng, H. (2014). Anatomical characterization of Cre driver mice for neural circuit mapping
655 and manipulation. *Frontiers in Neural Circuits*, 8. Publisher: Frontiers.
- 656 Hennig, C. (2007). Cluster-wise assessment of cluster stability. *Computational Statistics & Data
657 Analysis*, 52(1):258–271.
- 658 Horn, G. and Hill, R. M. (1966). Responsiveness to sensory stimulation of units in the superior
659 colliculus and subjacent tectotegmental regions of the rabbit. *Experimental Neurology*, 14(2):199–
660 223.
- 661 Hoy, J. L., Bishop, H. I., and Niell, C. M. (2019). Defined Cell Types in Superior Colliculus Make
662 Distinct Contributions to Prey Capture Behavior in the Mouse. *Current Biology*, 29(23):4130–
663 4138.e5.
- 664 Inayat, S., Barchini, J., Chen, H., Feng, L., Liu, X., and Cang, J. (2015). Neurons in the Most
665 Superficial Lamina of the Mouse Superior Colliculus Are Highly Selective for Stimulus Direction.
666 *The Journal of Neuroscience*, 35(20):7992–8003.
- 667 Isa, T., Marquez-Legorreta, E., Grillner, S., and Scott, E. K. (2021). The tectum/superior colliculus
668 as the vertebrate solution for spatial sensory integration and action. *Current Biology*, 31(11):R741–
669 R762. Publisher: Elsevier.
- 670 Ito, S., Feldheim, D. A., and Litke, A. M. (2017). Segregation of Visual Response Properties in the
671 Mouse Superior Colliculus and Their Modulation during Locomotion. *Journal of Neuroscience*,
672 37(35):8428–8443.
- 673 Kaifosh, P., Zaremba, J. D., Danielson, N. B., and Losonczy, A. (2014). SIMA: Python software for
674 analysis of dynamic fluorescence imaging data. *Frontiers in Neuroinformatics*, 8(80):1–10.
- 675 Kass, R. E. and Raftery, A. E. (1995). Bayes Factors. *Journal of the American Statistical Association*,
676 90(430):773–795.
- 677 Kerlin, A. M., Andermann, M. L., Berezovskii, V. K., and Reid, R. C. (2010). Broadly Tuned
678 Response Properties of Diverse Inhibitory Neuron Subtypes in Mouse Visual Cortex. *Neuron*,
679 67(5):858–871.

- 680 Langer, T. P. and Lund, R. D. (1974). The upper layers of the superior colliculus of the rat: A Golgi
681 study. *Journal of Comparative Neurology*, 158(4):405–435.
- 682 Lee, K. H., Tran, A., Turan, Z., and Meister, M. (2020). The sifting of visual information in the
683 superior colliculus. *eLife*, 9:e50678. Publisher: eLife Sciences Publications, Ltd.
- 684 Li, Y.-t., Turan, Z., and Meister, M. (2020). Functional Architecture of Motion Direction in the
685 Mouse Superior Colliculus. *Current Biology*, 30(17):3304–3315.e4.
- 686 Mairal, J., Bach, F., Ponce, J., and Sapiro, G. (2009). Online dictionary learning for sparse coding. In
687 *Proceedings of the 26th Annual International Conference on Machine Learning*, ICML '09, pages
688 689–696, Montreal, Quebec, Canada. Association for Computing Machinery.
- 689 Major, D. E., Luksch, H., and Karten, H. J. (2000). Bottlebrush dendritic endings and large dendritic
690 fields: Motion-detecting neurons in the mammalian tectum. *The Journal of Comparative Neurology*,
691 423(2):243–260.
- 692 May, P. J. (2006). The mammalian superior colliculus: laminar structure and connections. In
693 Büttner-Ennever, J. A., editor, *Progress in Brain Research*, volume 151 of *Neuroanatomy of the*
694 *Oculomotor System*, pages 321–378. Elsevier.
- 695 Pnevmatikakis, E. A. and Giovannucci, A. (2017). NoRMCorre: An online algorithm for piecewise
696 rigid motion correction of calcium imaging data. *Journal of Neuroscience Methods*, 291:83–94.
- 697 Reinhard, K., Li, C., Do, Q., Burke, E. G., Heynderickx, S., and Farrow, K. (2019). A projection
698 specific logic to sampling visual inputs in mouse superior colliculus. *eLife*, 8:e50697.
- 699 Rodieck, R. W. (1991). The density recovery profile: A method for the analysis of points in the plane
700 applicable to retinal studies. *Visual Neuroscience*, 6(2):95–111. Publisher: Cambridge University
701 Press.
- 702 Roska, B. and Meister, M. (2014). The retina dissects the visual scene into distinct features. In
703 Werner, J. S. and Chalupa, L. M., editors, *The new visual neurosciences*, pages 163–82. MIT Press,
704 Cambridge, MA.
- 705 Rosón, M. R., Bauer, Y., Kotkat, A. H., Berens, P., Euler, T., and Busse, L. (2019). Mouse dLGN
706 Receives Functional Input from a Diverse Population of Retinal Ganglion Cells with Limited
707 Convergence. *Neuron*, 102(2):462–476.e8. Publisher: Elsevier.
- 708 Roy, S., Jun, N. Y., Davis, E. L., Pearson, J., and Field, G. D. (2021). Inter-mosaic coordination of
709 retinal receptive fields. *Nature*, pages 1–5. Publisher: Nature Publishing Group.
- 710 Sahibzada, N., Dean, P., and Redgrave, P. (1986). Movements resembling orientation or avoidance
711 elicited by electrical stimulation of the superior colliculus in rats. *Journal of Neuroscience*,
712 6(3):723–733.
- 713 Sanes, J. R. and Masland, R. H. (2015). The Types of Retinal Ganglion Cells: Current Status and
714 Implications for Neuronal Classification. *Annual Review of Neuroscience*, 38(1):221–246.
- 715 Savier, E. L., Chen, H., and Cang, J. (2019). Effects of Locomotion on Visual Responses in the
716 Mouse Superior Colliculus. *Journal of Neuroscience*, 39(47):9360–9368. Publisher: Society for
717 Neuroscience Section: Research Articles.
- 718 Shekhar, K., Lapan, S. W., Whitney, I. E., Tran, N. M., Macosko, E. Z., Kowalczyk, M., Adiconis, X.,
719 Levin, J. Z., Nemesh, J., Goldman, M., McCarroll, S. A., Cepko, C. L., Regev, A., and Sanes, J. R.
720 (2016). Comprehensive Classification of Retinal Bipolar Neurons by Single-Cell Transcriptomics.
721 *Cell*, 166(5):1308–1323.e30. Publisher: Elsevier.
- 722 Sibile, J., Gehr, C., Benichov, J. I., Balasubramanian, H., Teh, K. L., Lupashina, T., Vallentin, D.,
723 and Kremkow, J. (2022). High-density electrode recordings reveal strong and specific connec-
724 tions between retinal ganglion cells and midbrain neurons. *Nature Communications*, 13(1):5218.
725 Number: 1 Publisher: Nature Publishing Group.

- 726 Wang, L., Sarnai, R., Rangarajan, K., Liu, X., and Cang, J. (2010). Visual Receptive Field
727 Properties of Neurons in the Superficial Superior Colliculus of the Mouse. *Journal of Neuroscience*,
728 30(49):16573–16584.
- 729 Warwick, R. A., Kaushansky, N., Sarid, N., Golan, A., and Rivlin-Etzion, M. (2018). Inhomogeneous
730 Encoding of the Visual Field in the Mouse Retina. *Current Biology*, in press(0).
- 731 Wassle, H., Peichl, L., and Boycott, B. B. (1981). Morphology and Topography of on- and off-Alpha
732 Cells in the Cat Retina. *Proceedings of the Royal Society of London. Series B, Biological Sciences*,
733 212(1187):157–175.
- 734 Wheatcroft, T., Saleem, A. B., and Solomon, S. G. (2022). Functional Organisation of the Mouse
735 Superior Colliculus. *Frontiers in Neural Circuits*, 16.
- 736 Yan, W., Laboulaye, M. A., Tran, N. M., Whitney, I. E., Benhar, I., and Sanes, J. R. (2020). Mouse
737 Retinal Cell Atlas: Molecular Identification of over Sixty Amacrine Cell Types. *Journal of
738 Neuroscience*, 40(27):5177–5195. Publisher: Society for Neuroscience Section: Research Articles.
- 739 Yonehara, K., Shintani, T., Suzuki, R., Sakuta, H., Takeuchi, Y., Nakamura-Yonehara, K., and
740 Noda, M. (2008). Expression of SPIG1 Reveals Development of a Retinal Ganglion Cell Subtype
741 Projecting to the Medial Terminal Nucleus in the Mouse. *PLOS ONE*, 3(2):e1533. Publisher:
742 Public Library of Science.
- 743 Zeng, H. and Sanes, J. R. (2017). Neuronal cell-type classification: challenges, opportunities and
744 the path forward. *Nature Reviews Neuroscience*, 18(9):530–546. Number: 9 Publisher: Nature
745 Publishing Group.
- 746 Zhang, Y., Kim, I.-J., Sanes, J. R., and Meister, M. (2012). The most numerous ganglion cell type of
747 the mouse retina is a selective feature detector. *Proceedings of the National Academy of Sciences*,
748 109(36):E2391–E2398.

749 **Acknowledgments**

- 750 Funding: M.M. was supported by grants from NIH (R01 NS111477) and from the Simons Foundation
751 (543015SPI). Y.-t.L was supported by a grant from the NEI (K99EY028640) and a Helen Hay
752 Whitney Postdoctoral Fellowship.
753 Competing interests: The authors declare no competing interests.
754 Data and code availability: The data and code that produced the figures are available in a public
755 Github repository <https://github.com/yatangli/Li-CellTypes-2023> and in a permanent
756 institutional repository <https://doi.org/x/x>.